Iowa State University
Digital Repository

Retrospective Theses and Dissertations

Iowa State University Capstones, Theses and Dissertations

2002

High growth rate deposition of hydrogenated amorphous silicon-germanium films and devices using ECR-PECVD

Yong Liu
Iowa State University

Follow this and additional works at: https://lib.dr.iastate.edu/rtd

Part of the Electrical and Electronics Commons

Recommended Citation
Liu, Yong, "High growth rate deposition of hydrogenated amorphous silicon-germanium films and devices using ECR-PECVD " (2002). *Retrospective Theses and Dissertations*. 396.
https://lib.dr.iastate.edu/rtd/396

This Dissertation is brought to you for free and open access by the Iowa State University Capstones, Theses and Dissertations at Iowa State University Digital Repository. It has been accepted for inclusion in Retrospective Theses and Dissertations by an authorized administrator of Iowa State University Digital Repository. For more information, please contact digirep@iastate.edu.

المنارة للاستشارات

www.manaraa.com

INFORMATION TO USERS

This manuscript has been reproduced from the microfilm master. UMI films the text directly from the original or copy submitted. Thus, some thesis and dissertation copies are in typewriter face, while others may be from any type of computer printer.

The quality of this reproduction is dependent upon the quality of the copy submitted. Broken or indistinct print, colored or poor quality illustrations and photographs, print bleedthrough, substandard margins, and improper alignment can adversely affect reproduction.

In the unlikely event that the author did not send UMI a complete manuscript and there are missing pages, these will be noted. Also, if unauthorized copyright material had to be removed, a note will indicate the deletion.

Oversize materials (e.g., maps, drawings, charts) are reproduced by sectioning the original, beginning at the upper left-hand corner and continuing from left to right in equal sections with small overlaps.

Photographs included in the original manuscript have been reproduced xerographically in this copy. Higher quality 6" x 9" black and white photographic prints are available for any photographs or illustrations appearing in this copy for an additional charge. Contact UMI directly to order.

ProQuest Information and Learning
300 North Zeeb Road, Ann Arbor, MI 48106-1346 USA
800-521-0600

UMI®

High growth rate deposition of hydrogenated amorphous silicon-germanium films and devices using ECR-PECVD

by

Yong Liu

A dissertation submitted to the graduate faculty

in partial fulfillment of the requirements for the degree of

DOCTOR OF PHILOSOPHY

Major: Electrical Engineering (Microelectronics)

Program of Study Committee:
Vikram Dalal, Major Professor
David Lynch
Joseph Shinar
Robert Weber
Gary Tuttle

Iowa State University

Ames, Iowa

2002

Copyright © Yong Liu, 2002. All rights reserved.

UMI Number: 3051487

Copyright 2002 by
Liu, Yong

All rights reserved.

UMI®

UMI Microform 3051487

Copyright 2002 by ProQuest Information and Learning Company.
All rights reserved. This microform edition is protected against
unauthorized copying under Title 17, United States Code.

ProQuest Information and Learning Company
300 North Zeeb Road
P.O. Box 1346
Ann Arbor, MI 48106-1346

Graduate College
Iowa State University

This is to certify that the Doctoral dissertation of

Yong Liu

has met the dissertation requirements of Iowa State University

Signature was redacted for privacy.

Major Professor

Signature was redacted for privacy.

For the Major Program

TABLE OF CONTENTS

ABSTRACT ix

CHAPTER 1. OVERVIEW 1

1.1 Physics of a-(Si,Ge):H alloys 2

1.1.1 Structure 2

1.1.2 Density of states 3

1.1.3 Electrical and optical properties 5

1.2 a-(Si,Ge):H application in solar cells 6

1.3 Literature review 8

1.4 Scope of research 11

CHAPTER 2. SAMPLE PREPARATION 14

2.1 ECR PECVD system 14

2.2 Growth chemistry 16

2.3 Modeling of solar cell device 19

2.3.1 Device configuration 19

2.3.2 Device modeling 20

CHAPTER 3. MATERIAL AND DEVICE CHARACTERIZATION 22

3.1 Film characterization methods 22

3.1.1 Thickness 23

3.1.2 Optical band gap 24

3.1.3 Urbach energy 27

3.1.4 Conductivity 30

3.1.5 Quantum efficiency mobility and life-time product ($\eta\mu\tau$) 31

3.1.6 Fourier-transform infrared (FTIR) measurement 32

3.2 Device characterization methods 34

3.2.1 I-V curve 35

3.2.2 Quantum efficiency 37

3.2.3 Hole $\mu\tau$ product 41

3.2.4 Space-Charge-Limited Current (SCLC) 42

CHAPTER 4. RESULTS AND DISCUSSION 47

4.1 The SCLC measurement results 47

4.1.1 Ion flux effect 51

4.1.2 He plasma 52

4.1.3 Discussion about the growth chemistry 53

4.2 General characteristics of a-(Si,Ge):H grown under high growth rate condition 56

4.2.1 The effect of pressure 57

4.2.2 The effect of substrate bias 62

4.2.3 The properties of the 15mTorr a-(Si,Ge):H material 64

4.3 Results of the a-(Si,Ge):H devices 67

CHAPTER 5. CONCLUSION 75

BIBLIOGRAPHY 77

ACKNOWLEDGEMENTS 85

LIST OF TABLES

Table 1.1 Some properties of typical a-Si:H and a-(Si,Ge):H 6

Table 3.1 Parameter A which relates the strength of the infrared bands of a-Si:H and a-Ge:H to the hydrogen concentration 34

Table 4.1 Substrate deposition pressure, film thickness, Hydrogen content vs ECR-PECVD film sample number 48

Table 4.2 Deposition parameters for pressure investigation 57

Table 4.3 Deposition parameters for biased substrate investigation 62

Table 4.4 Deposition parameters for high growth rate a-(Si.Ge):H devices . 68

LIST OF FIGURES

Figure 1.1 Illustration of continuous random network 3

Figure 1.2 DOS in $a - Si_{0.7}Ge_{0.3} : H$ [5] 4

Figure 1.3 Band diagram of the a-(Si,Ge):H devices 7

Figure 1.4 Structure of a typical p-i-n device 7

Figure 2.1 Schematic of ECR-CVD system 15

Figure 2.2 Detailed structure of p-i-n substrate solar cell 20

Figure 2.3 Equivalent circuit model of p-i-n device 21

Figure 3.1 Thickness extraction by transmission spectroscopy 23

Figure 3.2 Absorption constant, α, as a function of photon energy E determined from direct measurements of optical density. 25

Figure 3.3 Tauc energy derived from absorption coefficient 26

Figure 3.4 E04 energy derived from absorption coefficient 27

Figure 3.5 Apparatus for measuring sub-band gap absorption coefficients . 28

Figure 3.6 The abosorption coefficient vs incident photo energy 30

Figure 3.7 Schematic illustration of the bond-stretching(top row), bond-bending(middle row), and bond wagging (bottom row) modes of SiH, SiH_2 and SiH_3 grouping either in hydrogenated a-Si:H or gaseous silane 33

Figure 3.8 Current voltage characteristics of an illuminated p-i-n diode . . . 35

Figure 3.9 Quantum efficiency curve and quantum efficiency ratio curve . . 40

Figure 3.10 A simulation result of quantum efficiency against the experimental result 43

Figure 3.11 plot of current density J against applied voltage for a symmetric $n^+ - i - n^+$ specimen at room temperature. 44

Figure 3.12 Density of states calculated by differential method 46

Figure 4.1 Illustration of baseline subtraction: The height of the characteristic peaks, as well as the width of the peaks, have been changed after the base deduction. The interference fringes are nicely removed. The original data is on the top, the bottom graph is after baseline subtraction 49

Figure 4.2 The stretch mode and poly-hydride mode of two samples grown at 15mTorr and 5mTorr respectively. The Ge-H stretch mode is not obvious due to low Ge content. 51

Figure 4.3 The spectra of 5277 and 5293. Since the GeH_4/SiH_4 flow ratio is small. the 1890cm^{-1} Ge-H peak is not prominent. If take into account the baseline mismatch of the two curves, we could see that the two spectra overlap around 2000 cm^{-1} 55

Figure 4.4 FTIR spectrum of a-(Si,Ge):H films grown at high growth rate conditions, clearly showing the Ge-H peak around 1890cm^{-1} and the Si-H peak around 2000cm^{-1}. The prefactor can roughly be determined by the height of the peak. 56

Figure 4.5 (a) The conductivity vs pressure. (b) The Urbach energy vs. pressure. All the parameters were fixed except the pressure. . . . 58

Figure 4.6 $\mu\tau$ product vs pressure 60

Figure 4.7 Growth rate vs pressure 60

Figure 4.8 Pressure vs band gap. E04 as well as Etauc are given in this graph 61

Figure 4.9 The growth rate vs substrate bias 63

Figure 4.10 The defect density vs substrate bias 64

Figure 4.11 Conductivity vs band gap 65

Figure 4.12 Urbach energy vs band gap 66

Figure 4.13 Defect density vs band gap 67

Figure 4.14 Mobility life-time product vs band gap 68

Figure 4.15 The open-circuit voltage changed linearly with band gap. The thickness of the *i* layer and other deposition conditions except for the germane gas flow were kept as constant as possible to make sure that the open voltage only depends on the band gap. 69

Figure 4.16 The device performance drops due to the degradation of the materials 70

Figure 4.17 (a) Quantum efficiency and quantum efficiency ratio of sample 5582 which has band gap of 1.47 eV. (b) The quantum efficiency of devices at 420 nm and 700 nm. With more Ge incorporated into the devices, the quantum efficiency at longer wavelengths becomes larger. 72

Figure 4.18 Band diagram of graded band gap and graded doping a-(Si,Ge):H p-i-n solar cells. Solid line is with both graded band gap and graded doping, dashed line is only graded band gap. 73

Figure 4.19 I-V curves of samples 5585 and 5593 73

Figure 4.20 The quantum efficiency of samples 5585 and 5593 74

ABSTRACT

Hydrogenated amorphous silicon germanium films (a-SiGe:H) and devices have been extensively studied because of the tunable band gap for matching the solar spectrum and mature the fabrication techniques. a-SiGe:H thin film solar cells have great potential for commercial manufacture because of very low cost and adaptability to large-scale manufacturing. Although it has been demonstrated that a-SiGe:H thin films and devices with good quality can be produced successfully, some issues regarding growth chemistry have remained yet unexplored, such as the hydrogen and inert-gas dilution, bombardment effect, and chemical annealing, to name a few. The alloying of the SiGe introduces above an order-of-magnitude higher defect density, which degrades the performance of the a-SiGe:H thin film solar cells. This degradation becomes worse when high growth-rate deposition is required. Preferential attachment of hydrogen to silicon, clustering of Ge and Si, and columnar structure and buried dihydride radicals make the film intolerably bad. The work presented here uses the Electron-Cyclotron-Resonance Plasma-Enhanced Chemical Vapor Deposition (ECR-PECVD) technique to fabricate a-SiGe:H films and devices with high growth rates. Helium gas, together with a small amount of H_2, was used as the plasma species. Thickness, optical band gap, conductivity, Urbach energy, mobility-lifetime product, I-V curve, and quantum efficiency were characterized during the process of pursuing good materials. The microstructure of the a-(Si,Ge):H material was probed by Fourier-Transform Infrared spectroscopy. We found that the advantages of using helium as the main plasma species are: (1)High growth rate. The energetic helium ions break the reactive gas more efficiently than hydrogen ions. (2) Homogeneous

growth. Heavy helium ions impinging on the surface promote the surface mobility of the reactive radicals, so that heteroepitaxy growth as clustering of Ge and Si, columnar structure are reduced. (3)Surface hydrogen removal. Heavier and more energetic helium ions break the Si-H much easier than hydrogen ions. The preferential attachment of Si-H to Ge-H is reduced. We also found that with the small amount of hydrogen put into the plasma, the superior properties of a-(Si,Ge):H made from pure hydrogen dilution plasma were still maintained. These hydrogen ions help to remove the subsurface weakly bonded hydrogen and buried hydrogen. They also help to passivate the Ge- dangling bond.

High-quality material was successfully fabricated with the ECR-PECVD technique at high growth rates. Defect density lower than $2 \times 16\ cm^{-3}eV^{-1}$, Urbach energy less than 48 meV, and high mobility-lifetime were achieved. High-performance devices were made in the final state by using the optimal material we made. The device we made with 1.47 eV band gap has a fill factor of 64%. With the graded band gap and graded doping techniques, 70% fill factor was achieved when the band gap was graded from 1.75 to 1.47 eV. We also got 68% fill factor with the band gap graded from 1.75 to 1.38 eV.

CHAPTER 1. OVERVIEW

In the past years, the physics and technology of hydrogenated amorphous silicon (a-Si:H) have reached a degree of maturity which has made possible the use of this unique semiconducting material for an increasing number of applications [1]. Together with this development there has also been a growing demand for novel materials which are compatible with the present amorphous silicon technology. Therefore, the possibility of alloying amorphous silicon with other elements such as oxygen, nitrogen, carbon, or germanium has attracted more and more attention [2. 3]. Notably, amorphous silicon-germanium alloys(a-(Si,Ge):H) have been of much interest for the production of efficient solar cells, since the optical gap of these alloys can be easily tuned to match the solar radiation spectrum. Some other key features that make a-Si:H and a-(Si,Ge):H attractive photovoltaic materials are:

1. They have a very high optical absorption coefficient ($> 10^5 cm^{-1}$)over the majority of the visible spectrum, making extremely thin film (0.1-0.5 μm) devices possible, which implies low manufacturing cost.

2. A rather simple low-temperature deposition process can be used to coat uniformly an extremely large area.

3. The raw materials, i.e. silicon, germanium and hydrogen are abundant.

4. The material can be easily doped both p-type and n-type using boron or phosphorus sources, respectively.

5. Without the constraints of atomistic periodicity, amorphous materials can be deposited onto any foreign substrates with nonepitaxial heterostructure junctions.

6. Since the dangling bonds of amorphous a-Si:H or a-(Si,Ge):H could be compensated by hydrogen or fluorine, it might be possible to decrease the localized state density.

1.1 Physics of a-(Si,Ge):H alloys

Several deposition processes, such as CVD, PECVD, Photo-CVD, reactive sputtering, and others, can be used to produce amorphous silicon and amorphous silicon germanium for solar cells. In these techniques, hydrogen is either added or released during processing and incorporated into the deposited film. Hydrogenated films contain about 1 to 40 atomic percentage of hydrogen and are generally denoted by a-Si:H or a-(Si,Ge):H . Significant efforts have been made to study the physics of these materials.

1.1.1 Structure

In a perfect crystalline silicon structure, all four covalent bonds of an atom are saturated, and no unpaired spins show up in the ESR measurement. Structural models of covalently bonded amorphous silicon showed that the average number of next neighboring atoms is lower than four, so a certain fraction of atoms is only co-ordinated with three or less nearest neighbors. This model is called the continuous random network [1] as shown in Fig. 1.1.

In this tetrahedral network model, silicon atoms bond covalently to four neighboring silicon or germanium atoms with small deviations of the bonding lengths and angles from those of the crystalline material. The accumulation of the deviations eventually destroys the symmetry of the structure. Some Si or Ge atoms only have a coordination number of three, leaving one unpaired electron, which is known as a dangling bond. These dangling

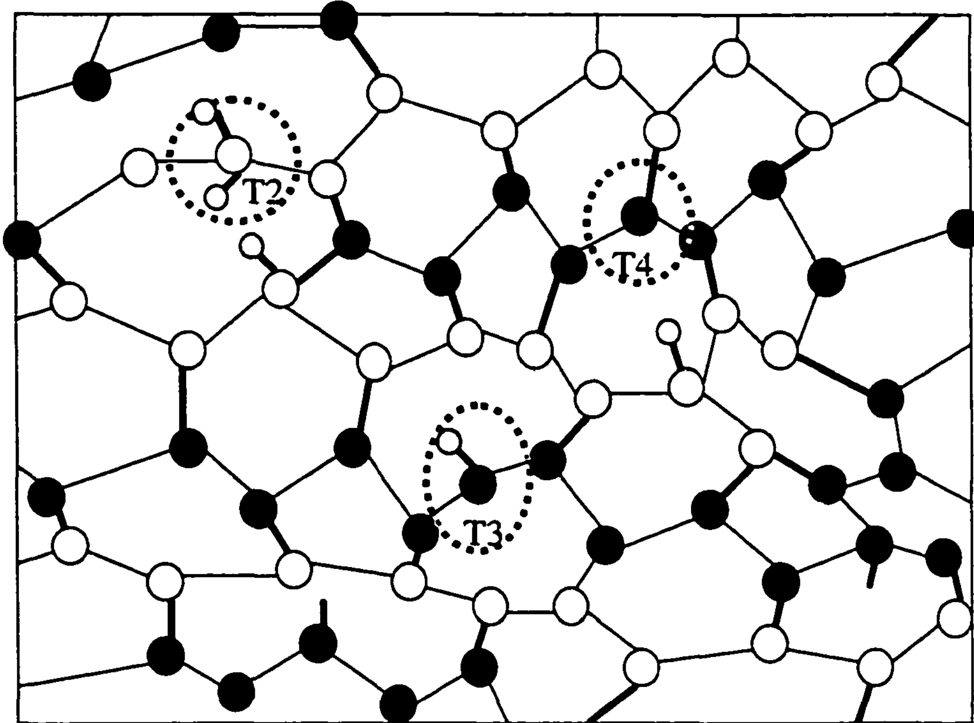

Figure 1.1 Illustration of continuous random network

bonds will act as recombination centers which are detrimental to solar cell performance. It was shown in the literature that before being passivated by hydrogen, the number of dangling bonds is about $10^{20} - 10^{22}$ cm^{-3}, while after the passivation, the number drops dramatically to about 7×10^{14} cm^{-3} for the best a-Si:H [4]. Both dangling bonds and deviations of the bonding lengths and angles will contribute to the formation of a continuous energy distribution of density of states.

1.1.2 Density of states

In order to obtain more insight into the electronic properties of amorphous silicon germanium, it is important to determine the distribution of the trap states in the band gap. Fig. 1.2 shows an electronic density of states of a-(Si,Ge):H obtained by Stutzmann [5].

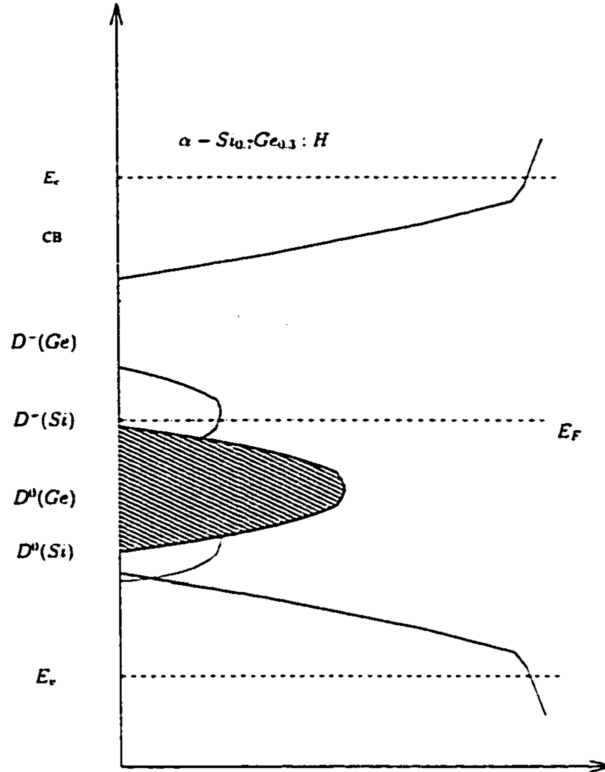

Figure 1.2 DOS in $a - Si_{0.7}Ge_{0.3} : H$ [5]

The lack of long-range order and distortion of the covalent bonds of fourfold co-ordinated neutral silicon atom in amorphous structure gives rise to a gradual, approximately exponential decrease of the density of states, so called band tails, given by

$$N_{TC} = N_{C0} \exp \frac{E_V - E}{E_{urc}} \tag{1.1}$$

$$N_{TV} = N_{V0} \exp \frac{E - E_V}{E_{urv}} \tag{1.2}$$

E_{urv} and E_{urc} are the characteristic widths of the conduction and valence band tails. The typical values for good a-Si:H are E_{urv}=42-45 meV, E_{urc}=26 meV [6]. These reverse values of the slope of the band tails are also called the Urbach energy, which can be used to determine the quality of the material. Low Urbach energy implies less disorder, which is a very important property of amorphous materials.

Adjacent to the band tail states are several deep-level bands in the lower and upper-half of the band gap, which are considered to be related to dangling bonds of mainly threefold co-ordinated silicon and/or germanium atoms. It is mostly assumed that the upper levels ($D^{-}(Si)$ or $D^{-}(Ge)$) correspond to the negatively charged dangling bonds, while the lower levels correspond to the positively charged or neutral dangling bonds.

It is believed that the degradation in properties of a-(Si,Ge):H alloys with decreasing band gap is due to the increasing micro-structure defects by the incorporation of Ge into the material. Mahan, Raboisson, and Tsu [8] suggested that in the case of Ge alloying of a-Si:H , there is a recombination channel other than through midgap defects and they correlated this excess recombination with the presence of microstructure (local disorder) as detected by infrared (IR) vibrational spectroscopy. Features such as columnar structure, void volume fraction, void size distribution, void shape, and heterostructure, although of micrometer scale, are often included in the concept of microstructure as well. Many of these attributes are interrelated, such as dihydride content and void fraction, clustered hydrogen and dihydride bonds, and clustered hydrogen and void fraction. Another aspect of poor structure is the presence of weak Si-Si, Si-Ge, Ge-Ge, Si-H or Ge-H bonds. For a-Si:H films deposited from silane, strained or weak Si-Si bonds may constitute 6-8% of all Si-Si bonds [7]. Breaking such bonds in films as a result of environmental factors, such as high temperature or light, deteriorates film quality because of an increase in dangling bond density; and such bond breaking may be the cause for the light-induced and thermally-induced instabilities.

1.1.3 Electrical and optical properties

Although a-(Si,Ge):H is currently the best low-band gap material, it has much poorer electrical and photoelectric properties than a-Si:H (for example, reduced photoconductivity and photoluminescence, and increased midgap density). The photoelectric properties deteriorate with increasing Ge content, and the deterioration proceeds rapidly as

the Ge content of the alloy exceeds 40% (corresponding to a band gap of approximately 1.5 eV) [2].

The optical and electrical properties of a-(Si,Ge):H are directly related to the Ge content of the alloy; as the Ge content, x, of $a - Si_{1-x}Ge_x : H$ increases from zero to 100%, there are some principal findings [2, 9, 10]. (1) As x is increased , the energy gap, E_{04} decreases linearly. (2) As x is increased , the magnitude of the photoconductivity response decreases rapidly.(3) As x is first increased to about 0.37, the magnitude of the sub band-gap absorption increases, until the effect is obscured at small values of the energy gap. (4) As x is increased, the infrared-vibrational-absorption spectra changes in a way suggesting structural alterations. (5) As x is increased, the space-charge limited current (SCLC) measurements suggests an increase in midgap DOS with increasing Ge content. The typical characteristics of a-Si:H and a-(Si,Ge):H under normal growth rate, especially prepared by glow discharge CVD, are listed in Table 1.1 [26].

Table 1.1 Some properties of typical a-Si:H and a-(Si,Ge):H

Property	**a-Si:H**	**a-SiGe:H**
Bandgap	1.7 to 1.8 eV	1.0 to 1.7 eV
Urbach energy	42 to 50 meV	$\geq$ 45 meV
Photoconductivity	10^{-4} S/cm to 10^{-5} S/cm	10^{-5} S/cm to 10^{-7} S/cm
Dark Conductivity	10^{-10} S/cm to 10^{-11} S/cm	10^{-9} S/cm-10^{-11} S/cm
$\mu\tau$ (hole)	$\geq 10^{-8}$ cm^2/V	10^{-8} to 10^{-10} cm^2/V

1.2 a-(Si,Ge):H application in solar cells

Hydrogenated amorphous silicon germanium alloys ($a - Si_{1-x}Ge_x$ or simply a-SiGe:H) are , so far, the only type of low-band gap materials used in multiple-junction amorphous silicon solar cells. The reason for the interest in multi junction devices is their potentially higher conversion efficiency than that of single-junction devices. For example, to achieve high efficiency in a-Si:H tandem cell structure with the high band gap material being

the standard 1.75 eV a-Si:H, the low-band gap material should have an optical band gap of less than 1.5 eV, preferably as low as 1.2 eV. Thus the higher-energy portion of the solar spectrum is absorbed by the top cell while the longer wavelength spectrum s absorbed by the low gap bottom cell. In a-Si:H single junction cell, the low energy part is wasted due to the low absorption coefficient. Fig. 1.3 shows the band diagram of the p-i-n devices(Fig. 1.4).

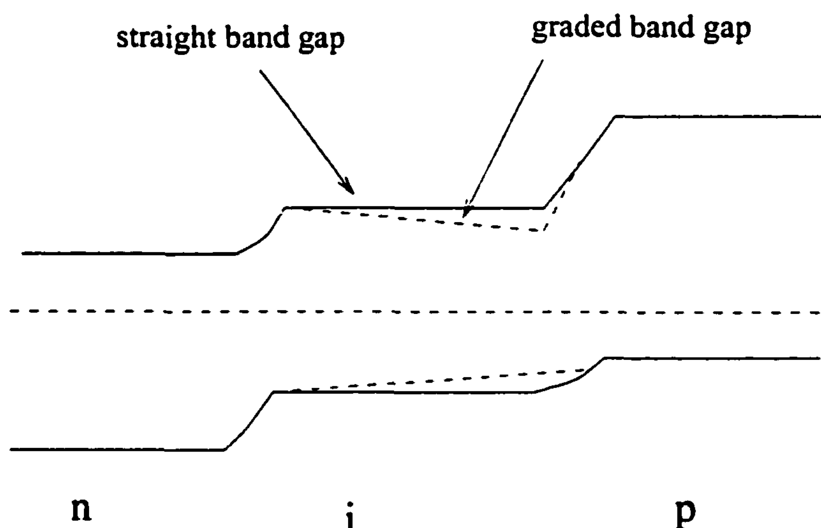

Figure 1.3 Band diagram of the a-(Si,Ge):H devices

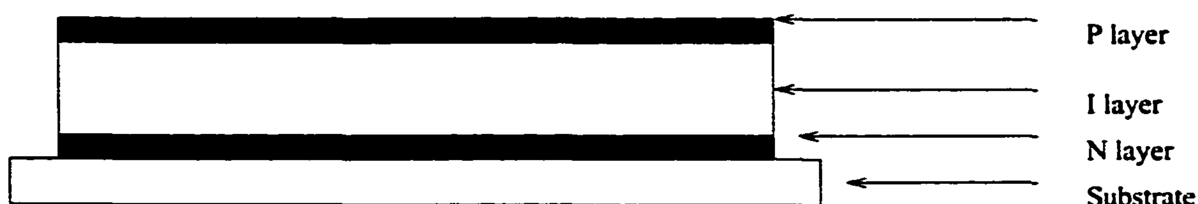

Figure 1.4 Structure of a typical p-i-n device

The solar cell devices in this project are fabricated on rough stainless steel substrates and are all p-i-n type, with light entering from the p side. The device structure consists of a thick back n a-Si:H layer (about 300-600 nm), followed by a thin graded-gap buffer layer which varies the band gap from that of a-Si:H to that of a-(Si,Ge):H . Next, an i layer

of a single band gap is deposited to the required thickness. This is followed by a thin, graded-gap buffer layer to increase the band gap from a-(Si,Ge):H to $p^+ - a - (Si, C) : H$ layer. A semi-transparent Cr contact completes the structure[11]. The light penetrates the p layer and is absorbed in the i layer. Electron-hole pairs are excited by the incident photons. Under the internal electric-field, the electrons are swept to the n layer and holes to the p layer. Thus the photo current is generated.

1.3 Literature review

Plasma-assisted chemical vapor deposition (CVD), also know as glow-discharge deposition, has become the most common technique used in the deposition of hydrogenated amorphous silicon(a-Si:H) material for semiconductor device applications. The best quality a-Si:H to date is deposited by the glow-discharge technique. Such material has high photosensitivity($\sim 1 \times 10^7$), low Urbach energy (42 meV), low midgap density of states (2×10^{15} cm^{-3}), and low electron-spin-resonance spin density. However, the conventional glow discharge deposition method has its limitations, including low deposition rates and poor-quality low-band gap alloy materials. In addition, there has been very little real improvement in recent years in the defect and photo-stability properties of glow-discharge-deposited a-Si:H films.

M. Stutzmann and co-workers have used RF-glow discharge CVD techniques to produce a-Si:H materials [5]. These samples were deposited in a capacitively coupled diode reactor. Pure SiH_4 and GeH_4 were employed as the reactive gases and, where applicable, were diluted with He, Ar, or H_2. Microprobe, Raman, FTIR ,PDS, NMR as well as ESR were performed to characterize the materials.

By studying the optical properties, the authors claimed that the density of midgap defect states acting as recombination centers increases strongly with increasing germanium content. The optical gap varies approximately linearly with the alloy composition

x (for $Si_{1-x}Ge_x$). The extent of the band-tail states, as deduced from the optical data is only weakly dependent on the alloy composition. It increased by about 30meV from pure a-Si:H towards $a - Si_{0.5}Ge_{0.5} : H$ (maximum chemical disorder).

Electron Spin Resonance (ESR) was used intensively in this research. It was shown that the decrease in the photoconductive properties of SiGe alloys with decreasing optical gap is mainly caused by the increase in the Ge dangling bond density. One has to find a way of avoiding preferential Ge deposition. Strong dilution in inert gases together with high power levels could help, however, they believed that ion bombardment would allow the deposition of high quality materials. Thus, it appears that other approaches are necessary for the deposition of good alloys.

A research group in United Solar System Corp. has produced SiGe:H films and devices by triode RF CVD [14]. The advantage of the triode configuration is that bombardment the radicals and dilution gases can be controlled. Ion bombardment of the film growing surface by applying an electric bias is known to be an effective way to modify the film growth mechanism. By controlling the flux and energy of the impinging ions, reactive species can be energized to find a favorable site and form a denser network.

Both a-Si:H and a-SiGe:H single junction p-i-n devices were deposited in a multi-chamber reactor using conventional RF plasma-enhanced CVD and triode CVD. In this study, gas mixtures of $Si_2H_6 + H_2$ and $Si_2H_6 + GeH_4 + H_2$ were used for device depositions, respectively. They have shown that positive ion bombardment does indeed have a beneficial effect on a-SiGe:H deposition at high growth rates. These materials have poor quality since the impinging species do not have enough time to find stable sites. In the diode mode, no appreciable bias effect is observed on the SiGe alloy cells.

However, according to Matsuda, ion bombardment was detrimental to the film quality [15]. In their experiments, diode and triode reactors were used for comparison. In the triode system, the glow-discharge plasma is produced only between the cathode and the mesh electrode. The substrate electrode is electrically grounded, and a minus dc bias is

applied on the mesh electrode against the substrate electrode. Thereby, ionic species are prevented from penetrating the mesh towards the substrate and the RF glow-discharge plasma is completely confined between the cathode and the mesh. By keeping the distance between the mesh and the substrate electrodes longer, radicals having shorter lifetimes such as SiH_x (x=0-2) and GeH_x (x=0-2) are eliminated through many collisions and only longer-lifetime radicals, SiH_3 and GeH_3 can reach the substrate surface, namely, the deposition by long-lifetime radicals is realized, which is supposed to result in more uniform films.

The photo and dark conductivity measurements gave different results for the two different systems. The photoconductivity of the diode film showed a rapid decrease with decreasing band gap, while the photoconductivity of the triode films is approximately two orders of magnitude higher. The infrared transmittance spectra of the films deposited by the two systems were also studied. The SiH_2 dihydride stretching-mode absorption as well as the SiH_2 scissors-mode absorption were clearly observed at 2100 cm^{-1} and around 850 cm^{-1}, respectively, in the diode film, while none of them were in the triode film. It indicates that the preferential attachment of H to Si atoms is fairly relaxed on the triode film.

From the discussion above, Matsuda's and Stutzmann's results gave opposite conclusions on the ion bombardment effects. There is a lot of other literature which also gives controversial conclusions as well . Further experiments in our research are necessary.

Hot-wire CVD is also known as catalytic thermal CVD [18] or evaporative surface decomposition. It gained much attention in recent years on high-growth-rate depositions. In this technique, the silane feed gas is decomposed by pyrolitic and catalytic reaction on a heated filament at a temperature of 1300-2600^oC. The silicon atoms deposited on the filament are then thermally evaporated onto the substrate located only a few centimeters away from the filament. Hydrogen atoms are also generated at the filament surface by thermal and catalytic dissociation of silane and hydrogen molecules. The

substrate temperature is 200-300^oC, which is similar to that used by conventional glow discharge deposition. The actual deposition is governed by a constant, the pressure distance (PD) product.

This *PD* product rule makes some issues on deposition. The PD product is typically around 30 mT $\cdot$ cm. When the distance(D) is large, polymerization of radicals occurs before they reach the substrate, while if the distance is short, the temperature of the substrate is heavily affected by the hotwire, since the hotwire is around 1500^oC but the substrate is only 200-300^oC. And, uniformity of the film is hard to achieve due to the short distance from the filament to the substrate. Another big problem with the hotwire is that there are no ions in these reactions; thus there is no beneficial effect of ion bombardment, especially for GeH_4. Matsumura [25] claimed that they got high photoconductivity at band gaps of 1.40 -1.45 eV. However, this result is questionable, since the tungsten-wire contamination is a big issue in hotwire deposition. And last, the preferential attchment of H to Si than to Ge is much more prominent in the films prepared by hotwire, which means that there are more Ge dangling bonds.

1.4 Scope of research

In light of the current state of research on a-(Si,Ge):H solar cells, this research is focused on the following issues.

Deposition rate is one of the important factors to increase the throughput and reduce the capital cost for photovoltaic production as previously mentioned in section 1.1. It is even more crucial for a-(Si,Ge):H because of the large amount of materials used in the solar cells and the high cost of germane gas. The best a-Si:H -based solar cells are made at a deposition rate of about 1 Å/s. Presently, the properties of the high-deposition-rate (greater than 1 Å/s) materials remain inferior to those deposited at 1 Å/s. The efficiency of the high-growth-rate solar cells, as a consequence, is lower than

that of those made at 1 Å/s cells. High growth rate materials, solar cells, and growth mechanisms have received great attention because of the technical importance. Various deposition techniques such as electron cyclotron resonance, microwave, modified-VHF, and HWCVD have been examined [1[illegible], 17, 19], but only a little work has been done. Hot-wire CVD is a promising method provided that we can solve the *PD* limitation and no ion problems which are addressed in the previous section. Another method used in our group is the ECR-PECVD [20]. By varying the growth condition and looking inside the growth chemistry, high-growth-rate with high-quality materials and solar cell devices are expected.

By using the ECR-PECVD to achieve high growth rate, the ion bombardment is inevitable since inert gas such as helium is used. As mentioned in the last section, Matsuda and Stutzmann's group had different results on the ion bombardment effect. In recent years, Guha [22] and Sugiyama [21] pointed out that the ion bombardment is beneficial only when the material is less than optimum and heavy bombardment is detrimental to the properties of material due to the bombardment-induced defects. However, if we don't apply the ion bombardment effect, how can we know that the material can not be further optimized? One goal of this project is to study how to get optimized material with the help of ion bombardment. Unlike the regular growth-rate deposition, less hydrogen is used in the high-growth-rate process. However, hydrogen dilution has proved to be an important factor affecting the properties of the a-(Si,Ge):H materials [23, 24]. Little work has been done on the high growth rate which is believed to be much worse due to the smaller hydrogen dilution. Then another purpose of this research is to investigate the hydrogen-dilution effect; how does it affect the properties of the materials.

As summarized in previous sections, the quality of the materials can be characterized by three types of important measurements: the Urbach energy, the space-charge limited current (SCLC) and Fourier-transform infrared spectroscopy (FTIR). The Urbach energy

deals with the band tails; the SCLC characterizes the density of midgap; and the FTIR gives a rough image of the microstructure in the materials. In this research, these three types of measurements were systematically performed. Other important measurements such as conductivity and $\mu\tau$ product are investigated as well.

The ultimate goal of this research is to fabricate high-performance a-(Si,Ge):H devices. Various straight band gap and graded band gap devices were made with different Ge content combining the hydrogen dilution and ion bombardment control to obtain good a-(Si,Ge):H devices under high-growth-rate.

CHAPTER 2. SAMPLE PREPARATION

2.1 ECR PECVD system

In recent years, electron cyclotron resonance (ECR) plasma sources have been widely used in plasma and ion beam technologies. The growing interest in ECR CVD technology is motivated by the unique features of the ECR plasma which are superior to those of conventional RF plasma sources used in PECVD. Fig. 2.1 is a schematic of a typical system adopted by NTT [27]. A divergent magnetic field generated by coils surrounding the plasma excitation chamber extracts charged species of the plasma from the excitation chamber into the deposition chamber. The feed-stock gas is introduced in the deposition chamber where the extracted energetic gas species decompose the feed gas (indirect feed-gas decomposition). The excitation chamber operates as a microwave cavity resonator. The magnetic flux density in the excitation chamber is controlled to achieve the circular motion of electrons (ECR) in a region inside the excitation chamber. The plasma production efficiency is enhanced by satisfying the ECR condition, in which the electron cyclotron frequency (the frequency of the circular motion) is equal to the microwave frequency [27]. More than 70% of the microwave power is absorbed by the plasma. The microwave power required to sustain a stable plasma is reduced by one order of magnitude with respect to non-magnetically confined plasma. A microwave plasma operating under ECR conditions can increase the dissociation rate of molecular gases with the presence of high-energy electrons, while the gas temperature remains low because of inefficient energy transfer between electrons and heavier parti-

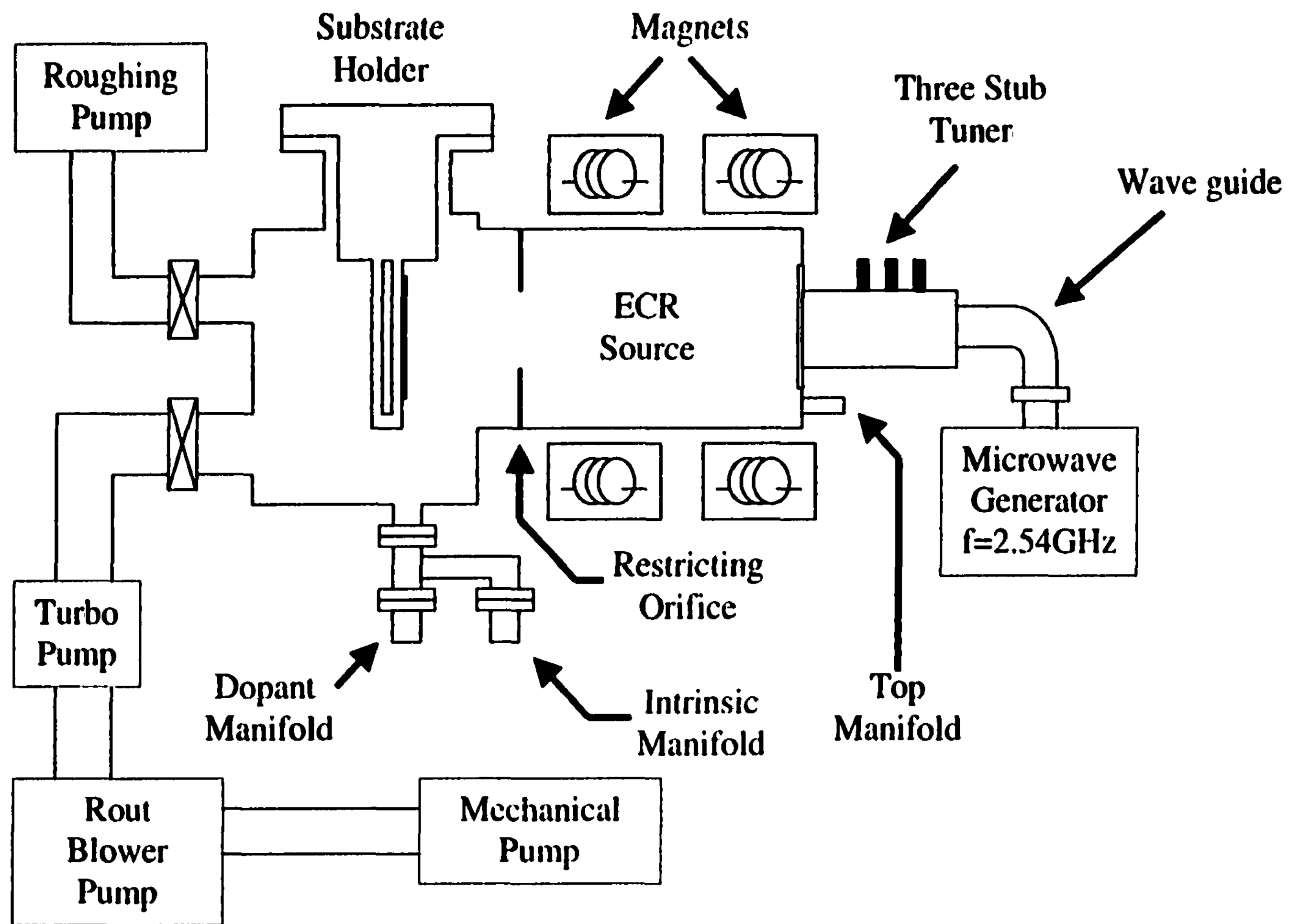

Figure 2.1 Schematic of ECR-CVD system

cles. The frequency of the microwave energy source is 2.45 GHz, which gives a resonance for 874-Gauss magnetic flux density.

Both the electron density and the electron temperature for ECR-CVD are high compared to those of a conventional RF glow discharge. The minimum gas pressure allowing the generation of plasma is much lower under ECR conditions than under conventional RF discharge. This is because the threshold pressure strongly decreases (by almost an order of magnitude) as the magnetic field approaches the ECR condition.

The advantage of the ECR microwave remote plasma CVD compared to convention glow discharge deposition are (1) efficient energy transfer from the microwave field to the plasma; (2) Easy control of the ion energy (typically 10-50 eV) by the gas pressure to avoid high-energy particle bombardment of the growing films. Thereby it produces less stress in the film and less damage to the growing surface; (3) High utilization of feed stock gases; (4) better control of the dissociation of the deposition gas; (5) lower operating pressures, which may lead to cleaner processing; (6) lower substrate temperature; (7) reduced powered electrode effects, such as contamination, self-biasing, and hot electron generation; (8) high ionization ratio and (9) high plasma density.

2.2 Growth chemistry

Growth chemistry plays a major role in the deposition of high quality material using plasma deposition [11]- [33]. For high growth rate deposition, one cannot make a good material without acknowledging the growth chemistry. For example, very high growth rates were obtained with the hot wire technique [34], but the degradation of high quality hot wire devices is significantly worse than the degradation of devices deposited using the glow discharge technique at lower growth rates. Similarly, one can get very high growth rates with a thermal plasma technique, but the device quality is still not very good. Achieving high growth rates with standard plasma deposition techniques,

particularly for a-(Si,Ge):H , presents problems related to stability and poorer device properties [35] as well, which is usually related to the presence of a high void density. Y. S. Tsuo at NREL found that films deposited with He dilution of SiH_4 and GeH_4 have higher mobility lifetime product ($\mu\tau$) and longer diffusion length (L_d) [36]. Similarly, according to our research efforts, the addition of inert gas bombardment by mixing H and He or H and Ar in a remote ECR plasma system has been shown to improve the device properties at high growth rates. The fundamental questions that arise then are why is it that some techniques seem to work better than others, and how to improve the growth rates while maintaining device properties.

In the ECR PECVD system, there are several reactions near the surface of the substrate:

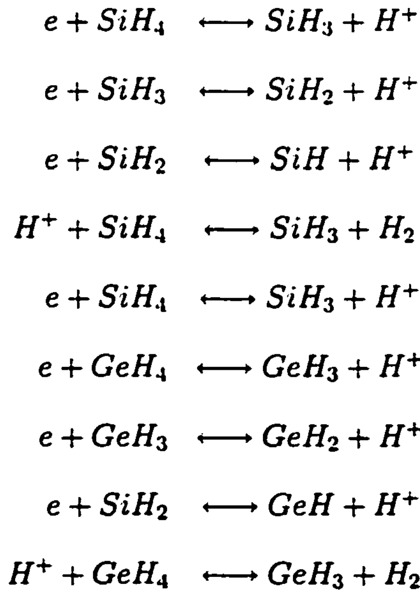

$$
\begin{aligned}
e + SiH_4 &\longleftrightarrow SiH_3 + H^+ \\
e + SiH_3 &\longleftrightarrow SiH_2 + H^+ \\
e + SiH_2 &\longleftrightarrow SiH + H^+ \\
H^+ + SiH_4 &\longleftrightarrow SiH_3 + H_2 \\
e + SiH_4 &\longleftrightarrow SiH_3 + H^+ \\
e + GeH_4 &\longleftrightarrow GeH_3 + H^+ \\
e + GeH_3 &\longleftrightarrow GeH_2 + H^+ \\
e + SiH_2 &\longleftrightarrow GeH + H^+ \\
H^+ + GeH_4 &\longleftrightarrow GeH_3 + H_2
\end{aligned}
$$

It is believed that SiH_3 and GeH_3 are dominant and the most important radicals (90%). They have higher surface mobility and low sticking coefficients. If the content of other radicals, such as SiH_4 , SiH_2 ,GeH_4 or GeH_2 , is high in the plasma, the surface will be rough and many dangling bonds and microvoids will be formed [4].

The standard model of a-Si:H growth according to Matsuda [37], Perrin [38], and

Gallagher [39] states that the growth of a-Si:H and a-(Si,Ge):H is limited primarily by surface diffusion of a radical such SiH_3 . When this radical finds an open site, it bonds, and H is eliminated by breaking of Si-H bonds and subsequent cross-linking of neighboring hydrogens' bonded to adjacent Si atoms. However, a silyl radical bonded to a surface Si is relatively stable; it is almost like a silane molecule. There is no reason for a Si-H bond to break from such a surface-bonded radical at typical growth temperatures since the bond breaking energy is around 2.5 eV. Therefore, some other mechanism must be responsible for removing this H. V. Dalal [32] improved this model. He suggested that the primary consideration which determines the growth of high quality a-Si:H and alloy films is not surface diffusion *per se*, but rather the removal of surface hydrogen, and this removal takes place not by reactions between neighboring H bonded to adjacent Si atoms, but rather, by extraction of hydrogen by H radicals and inert gas ions. A high H dilution leads to a significant concentration of H ions and radicals impinging on the surface, and these remove the bonded H. The H ions also penetrate deeper into the lattice, and remove some more bulk H. The role of inert gas ions, such as Ar and He is to break the surface H bonds, thereby creating a dangling bond, and allowing another silyl radical to insert itself. The inert gas ions do not penetrate deep into the substrate, but H ions do. If the surface hydrogen is not removed, and Si not cross-linked, the bonded Si-H structures get buried, new material grows around it, and a microstructure with a significant void concentration and clustered silicon-hydrogen bonds form in the lattice. Such microstructure then leads to rapid degradation.

With the addition of Ge, the degradation becomes worse due to the microstructures mentioned in the previous sections. It is believed to arise from the following reasons: (1) Growth from many radicals; the inhomogeneous growth leads to poor microstructures. (2) Ge is heavier than Si, so the surface mobility of Ge is very low. This results in the heterostructure epitaxy. (3) The Si-Si bond (2.3 eV) is stronger than Ge-Ge bond (1.9 eV), so there is a preference for incorporation of Ge over Si, similarly, the Ge-H bond

(2.99 eV) is weaker than the Si-H bond (3.35 eV), so there are more Ge dangling bonds.

The question that arises is: how does one improve the quality of a-(Si,Ge):H alloy under high growth rates? Most experiments suggest that the fundamental limitation on the growth of good-quality a-Si:H is how rapidly the excess H is eliminated from the surface. Ion bombardment is also critical for improving the mobility of radicals on the surface, particularly for the case of a-(Si,Ge):H . Bombardment by inert gas ions can enhance the elimination of excess H at the surface, thereby reducing the probability of forming microvoids in the films. So far, the basic techniques are hydrogen dilution, biased substrate (ion bombardment control), inert gas dilution (high growth rate, ion bombardment) and, of course, some basic process control, such as temperature and pressure control.

2.3 Modeling of solar cell device

2.3.1 Device configuration

The basic structure of a p-i-n device is discussed in the previous chapter. The detailed structure is illustrated in Fig. 2.2. The process of device fabrication is called layer by layer (LBL) technique. The I2 layer is the dominant layer, which absorbs most solar energy while I1 is a thin and graded SiC layer. The functionality of the I1 layer can be divided into three categories: (1) The transition layer, which smooths out the band gap and lattice mismatch with the p^+ layer which is also SiC. (2) The boron blockage layer. The p layer is heavily doped with boron, and boron diffusion can cause very serious problem in modern semiconductor process. For example, extra boron will introduce defective states in the lattice. Fortunately, SiC is a very good at blocking the diffusion of boron. (3) High electric field. There is no doubt that the interface (p to i) is very defective which means that the recombination around this region is very high. The high electric field caused by a graded band gap could sweep out the excess carriers faster, in

other words, reduce the probability of recombination close to the interface.

The p layer is also a combination of three thin layers (P1, P2, and P3). In general, the purpose of P1 is similar to I1 but it is doped with boron. The P2 layer is a low resistivity microcrystalline layer. According to the circuit model, high resistivity will limit the output of the solar cell and consume energy. By using high mobility microcrystalline si, the series resistance is greatly reduced. P3 is also heavily doped with boron to form a better ohmic contact with Cr metal on top. In this project, a Cr film instead of ITO is used as electrode. This 100 Ålayer will let 20% light through. Above the Cr dot is a thin and 1000 Åthick aluminum bar that acts as a probe point to protect the Cr layer from been punched through during the electrical measurement.

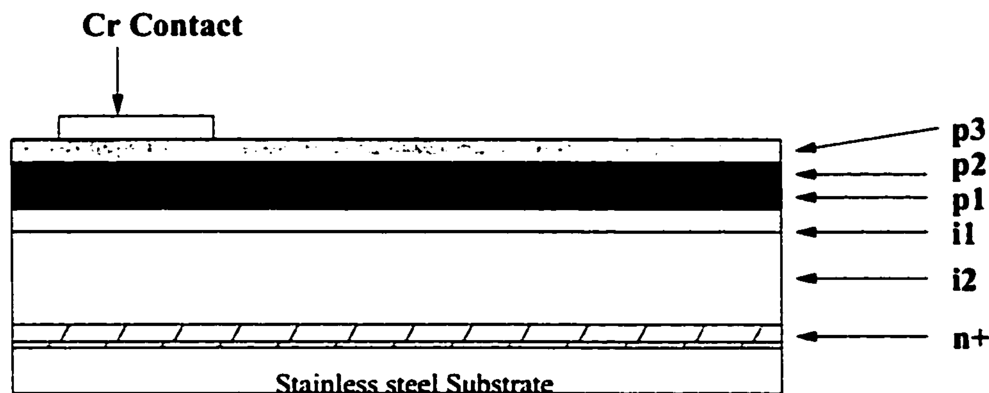

Figure 2.2 Detailed structure of p-i-n substrate solar cell

2.3.2 Device modeling

The equivalent circuit of the device is shown in Fig. 2.3.2. The ideal model does not include the shunt and series resistor. JL is the current source which simulates the generation of the photocurrent in the p-i-n junction. The series resistance is due to the bad p layer or bad metal contact on top of the p layer. The low shunt resistance is caused by the poor properties of the i layer, such as midgap density and microstructure. Generally, every device has shunt and series resistance. This research goal, in terms of

the circuit model, is to reduce the series and increase the shunt resistance. This model will be used in the later charpter for improving the performance of solar cells.

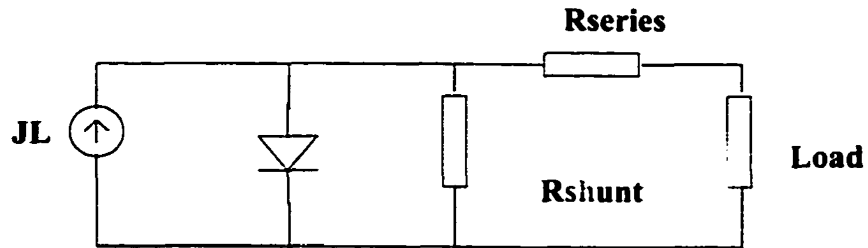

Figure 2.3 Equivalent circuit model of p-i-n device

CHAPTER 3. MATERIAL AND DEVICE CHARACTERIZATION

The chemical, structural, and electronic properties of the a-(Si,Ge):H films and devices made in this work have been characterized using a variety of techniques . Quantitative and qualitative measurements of the a-(Si,Ge):H films were obtained using a UV/VIS/NIR $\lambda - 9$ spectrometer, FTIR, dual channel lock-in amplifier, and HP X-Y recorder. Material properties that were measured include the film thickness, growth rate, Tauc band gap, E_{04} band gap, conductivity, hydrogen bonding, absorption coefficient, Urbach energy, and electrons $\mu\tau$ product whereas the solar cell devices properties that have been measured include the I-V curve, quantum efficiency, defect density, holes $\mu\tau$ product.

3.1 Film characterization methods

Film characterization techniques were used to obtain the properties of the a-(Si,Ge):H thin films. The film properties measured through optical characterization include the thickness, the conductivity, the absorption, the subgap absorption, the bonding present, as well as the E_{04} and Tauc band gaps. A comprehensive review of optical characterization methods for sëmiconductor materials can be found in the literature [40].

3.1.1 Thickness

The thickness of the silicon films can be determined from the period of the oscillations in the transmission versus the wavelength curve in the 1000 to 2500 nm region by using the equation

$$t = \frac{i}{2n_1\Delta(1/\lambda)} = \frac{i\lambda_i\lambda_o}{2n_1(\lambda_i - \lambda_o)}, \tag{3.1}$$

where i is the number of complete cycles from λ_o to λ_i which are the wavelengths of peaks of the i cycles. Fig. 3.1 shows the transmission of films which can be used to extract the thickness.

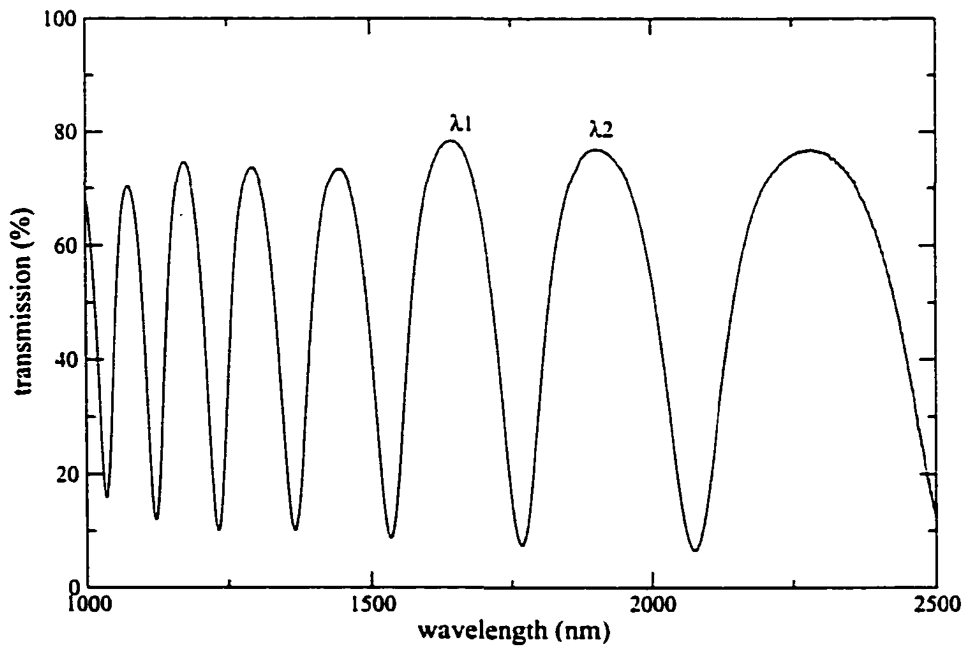

Figure 3.1 Thickness extraction by transmission spectroscopy

The index of refraction of the amorphous sample is assumed to be 3.5-3.6 over this wavelength range. For $a - Si_{1-x}Ge_x$, the index varies with x and can be extracted from

a lookup table or an empirical curve. It is also possible to acquire a more accurate value for the index of refraction by obtaining the reflection spectra of the film and solving for n_1 in the expression

$$Avg(R) = \frac{(n_1 - n_0)^2}{(n_1 + n_0)^2}, \tag{3.2}$$

where $Avg(R)$ is the average reflection in the non-absorbing range. Although the index of refraction varies with wavelength, its variation within this range is small enough to be considered a constant value.

3.1.2 Optical band gap

The spectral region of major interest for a semiconductor is in the vicinity of the absorption edge, since it can provide information on the optical gap, E_g, as well as on the density of states within the gap. Fig. 3.2 illustrates the absorption coefficient versus photon energy. There are three major regions of interest, A, B and C, as indicated in Fig. 3.2; these are discussed below and in the next subsection.

In considering region A we recall that in crystalline materials there are two types of optical transitions that can occur at the fundamental absorption edge, direct and indirect. Both involve the absorption of an electromagnetic wave by an electron in the valence band that is raised above the forbidden gap to the conduction band. However, indirect transitions involve the simultaneous interaction with phonons. For indirect band material, the absorption coefficient is given by

$$\alpha\hbar\omega = B(\hbar\omega - E_g)^n, \tag{3.3}$$

where n=2 or 3, depending on whether the transition is quantum mechanically allowed or forbidden (Actually, it's more complicated than this). The prefactor B is a constant which is determined by the intrinsic properties of the material. Equation (3.3) is generally used for a-(Si,Ge):H alloys with n=2 and implicitly assumes parabolic bands and equal matrix elements for all optical transitions for photon energies in excess of the band

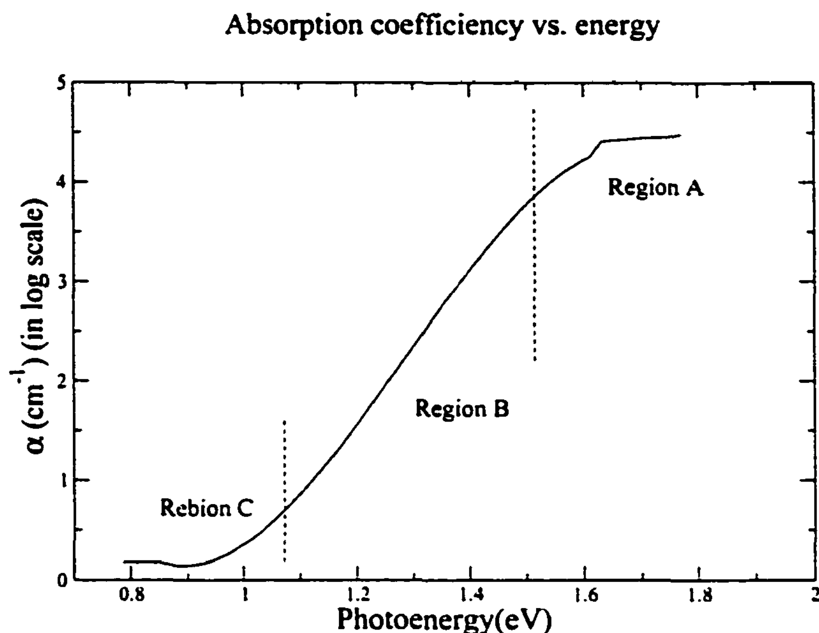

Figure 3.2 Absorption constant, α, as a function of photon energy E determined from direct measurements of optical density.

gap. Optical band gap deduced by this equation is called the Tauc energy [41] (E_{tauc}). E_{tauc} can be determined by plotting $(\alpha\hbar\omega)^{1/2}$ as a function of the energy of the incident photons, $\hbar\omega$ which is shown in Fig. 3.3. This plot yields a straight line which can be extrapolated to the x-axis to determine the Tauc gap. Amorphous silicon typically has a value of 1.75 eV for E_{tauc} whereas a-(Si,Ge):H tends to have various value from 0.9-1.7eV depending on the content of germanium.

Another parameter for characterizing the optical band gap is called E_{04}. Fig. 3.4 is a typical absorption curve measured by the Perkin Elmer lambda 9 UV/VIS/NIR spectrometer. The knee of the absorption curve typically occurs around $\alpha(E) = 10^3$ to 10^4cm^{-1} which is denoted as the E_{03} or E_{04} energy gap, respectively [42]. The difference between E_{04} and E_{tauc} is that the former is thickness independent. Typically, there is 0.15-0.2 eV difference between them.

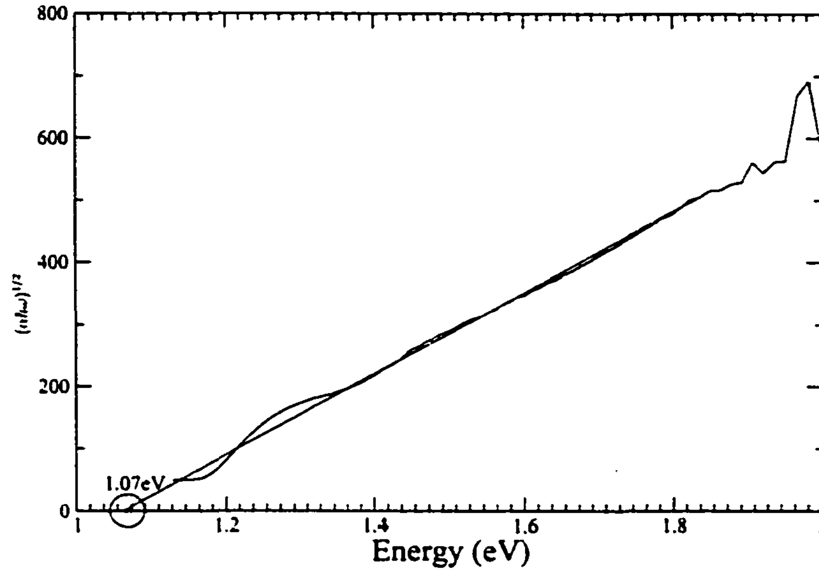

Figure 3.3 Tauc energy derived from absorption coefficient

The absorption coefficient as a function of wavelength can be calculated using the following expressions for the absorption and transmission as a function of the wavelength of the incident photons

$$T(\lambda) \approx (1 - R(\lambda))e^{-\alpha(\lambda)t}, \tag{3.4}$$

$$A(\lambda) = \log_{10} \frac{I_t}{I_i} = \log_{10} \frac{1}{T(\lambda)}, \tag{3.5}$$

where A(λ) is called optical density, T(λ) is the transmission and t is the thickness of the film, and $\alpha(\lambda)$ is the absorption coefficient. The absorption coefficient as a function of the wavelength can be calculated by combining the expressions for A(λ) and T(λ) and solving for the value of $\alpha(\lambda)$, which is found to be

$$\alpha(\lambda) = \frac{2\ln(1 - R(\lambda)) + 2.303A(\lambda)}{t}. \tag{3.6}$$

The Perkin Elmer Lambda 9 UV/VIS/NIR spectrophotometer was used to measure the reflection, transmission, and absorption characteristics of the a-(Si,Ge):H films that were

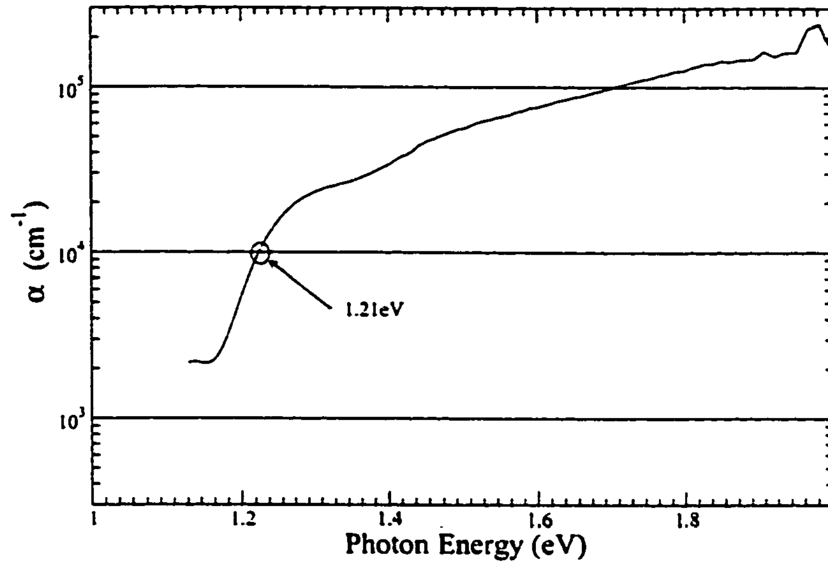

Figure 3.4 E04 energy derived from absorption coefficient

deposited in this work. The films were deposited onto Corning 7059 glass to perform measurements using the lambda 9. The transmission spectra of the films were measured from 1000-2500 nm, and the reflection and optical density spectra were measured over the 400 to 1100 nm range.

3.1.3 Urbach energy

Most amorphous semiconductors also have an exponential region B, as shown in Fig. 3.2. This region is referred to as the "Urbach tail" [43] and several mechanisms have been proposed to explain it, such as band gap variations due to density fluctuations, broadening of the band edge, or the presence of excitonic states induced by internal electric fields. Al Jalali *et al.* [45], from electro-absorption studies of a-Si:H, suggested that the absorption edge reflects the tailing of states into the gap region due to the fluctuations of bond lengths and bond angles. In addition, they proposed that the

transition probability changes rapidly in the absorption tail as the energy states become increasingly localized. It has also been suggested by many authors [41]- [44] that this tail could arise from electronic transitions between (localized) states in the band-edge tails, the density of which is assumed to fall off exponentially with energy. The expression is already described as equation 1.1 1.2 which is repeated here,

$$\alpha = \alpha_0 \exp \frac{h\nu - E_g}{E_{ur}}. \tag{3.7}$$

The two-beam photo-conductivity sub-band gap absorption technique developed by Wronski and co-workers [46], accurately probes the absorption sub-gap states below $\alpha = 10^2 cm^{-1}$. Since the majority of films prepared by the ECR-CVD technique are less than 10 μm thick, thin film geometry limits the accurate determination of α from absorption and reflection data taken by the spectrophotometer to $\alpha's$ greater than 10^2 cm^{-1}.

This two-beam photo-conductivity technique utilizes a DC light beam (or low frequency room light) to fix the quasi Fermi levels (and hence carrier lifetimes), while an AC light beam of low intensity probes the photoconductivity of the sample (see Fig. 3.5). More specifically, the DC beam continuously creates electron-hole pairs that

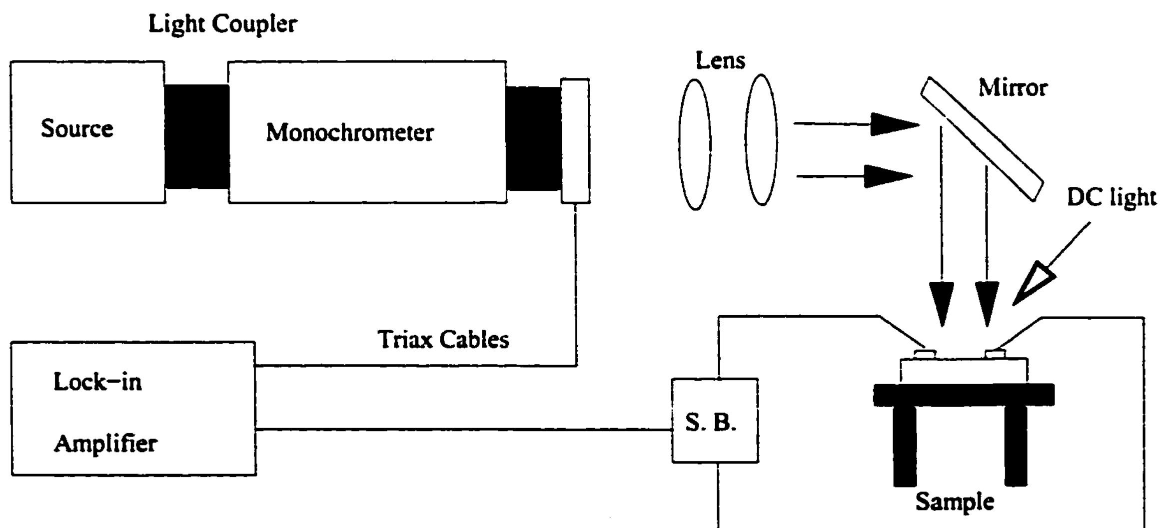

Figure 3.5 Apparatus for measuring sub-band gap absorption coefficients

keep the traps filled and the occupancy of the mid-gap states constant. This fixes the lifetimes of the photo-generated carriers. Meanwhile, the AC beam superimposes on the DC beam and thus modulates the creation of additional electron-hole pairs that can be detected by a lock-in amplifier. This photo-generated signal can be used to determine the absorption coefficient. To enhance the measured signal, a bias of 8 volts is placed across the sample to improve the transport of electron-hole pairs. The absorption coefficient is calculated at each wavelength by dividing the signal by a reference signal and multiplying by the quantum efficiency of the Si and Ge reference detector.

In the experimental apparatus shown in Fig. 3.5, the source is a white light and the monochromator is used to change the wavelength of the incident photons. The range of wavelengths used in the measurement is 600nm to 1600 nm for a-(Si,Ge):H films. Chopping the output of the monochromator at 13.5 Hz creates the AC beam. This frequency produces a square wave and reduces the noise due to ambient light. High pass optical filters are added at 700, 900 and 1220 nm to reduce second harmonics from the monochrometer and to prevent photons of shorter wavelengths from reaching the sample. The AC beam is collimated using two lenses and focused down onto the sample between the probe contacts with a mirror. Since the lifetime of the electron-hole pairs is constant, due to the DC light, the photo current corresponds directly to the absorption coefficient. Also, since the signal is detected with a lock-in amplifier only the photo current corresponding to the chopper frequency is detected. The Urbach energy is obtained by plotting the α(log scale) vs. energy. For a-(Si,Ge):H , since we do not know the exact composition, the curves are normalized by assuming the absorption coefficient at Tauc gap is about 1500 cm^{-1}. In this measurement, we assume that the mobility lifetime product ($\mu\tau$) of excess carriers are constant, so that the photo current is proportional to the absorption coefficient. In order to maintain a constant $\mu\tau$, or in other words, a constant excess carrier density, a neutral density filter was added where the incident photon energy is close to or above the band gap, since in that range, the

absorption is prominent and more excess carriers are generated. The film quality can be qualitatively determined by the Urbach energy. Usually, good films have small values. For example, the best a-Si:H film has 42 meV, while the best a-(Si,Ge):H varies from 45 meV to 51 meV. Fig. 3.6 shows the absorption curve deduced from this method. The fluctuation of the curve is due to the thickness interference which can be smooth out using moving average method.

The region C in Fig. 3.2 is due to the mid-gap states absorption.

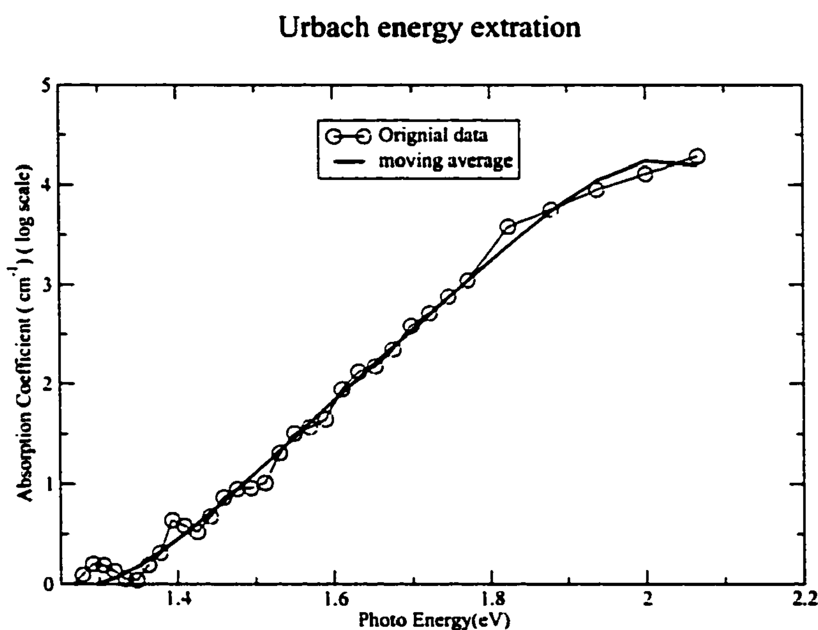

Figure 3.6 The abosorption coefficient vs incident photo energy

3.1.4 Conductivity

The photoconductivity measurement in our lab is performed by measuring the photo current under 1.5 Air-mass (AMS) lamp. The following equation is used to exact the

conductivity:

$$\sigma_{l,d} = \frac{L}{W} \cdot \frac{I}{V \cdot d}, \tag{3.8}$$

where L/W is the length to width ratio of the metal contact, d is the thickness of the film and V the applied voltage and I the photo current. Carriers in good films have less probability to be trapped so that the photoconductivity is large. The ratio of the photoconductivity to dark-conductivity is called the photo-sensitivity. Photo-sensitivity is sometimes used to determine whether the material is amorphous or microcrystalline since our ECR-PECVD is capable of making both of the samples. Microcrystalline material has smaller photosensitivity because it has a large intrinsic conductivity (dark conductivity). The photosensitivity also can help us to determine a material is contaminated (doped) or not because doping produces excess carriers, so that it has higher dark conductivity. However, the photosensitivity is the same or lower because of the defects introduced by the doping will reduce the lifetime of the excess carriers.

3.1.5 Quantum efficiency mobility and life-time product ($\eta\mu\tau$)

The photo-conductivity normalized against the actual amount of light absorption is equal to the product of the quantum efficiency, the mobility and the lifetime product. The simplest form of photoconductivity can be expressed as

$$\sigma_{ph} = \Delta n q \mu, \tag{3.9}$$

where

$$\Delta n = G \cdot \tau = \alpha(1 - R)\eta\tau\phi_{in}, \tag{3.10}$$

In other words,

$$\sigma_{ph} = \alpha(1 - R)\phi_{in} q \eta\mu\tau. \tag{3.11}$$

Here, ϕ_{in} is the amount of incident photons and G is the generation rate. Due to the large amount of surface absorption, the conductivity measurement is not accurate if

not taken under filters. A band-pass filter can only let specific range wavelength light pass through which can be calibrated through a standard reference cell. If the passed photons' energy is higher than the band gap of the film, the bulk absorption coefficient is also much large, so that the effect of surface absorption is reduced or minimized.

3.1.6 Fourier-transform infrared (FTIR) measurement

Fourier-transform infrared spectroscopy is a very informative tool to inspect the composition, the microstructure, and the content of materials. It is used in our lab to determine the H contentand the silicon-hydrogen and germanium-hydrogen bonding configurations. When photons in the mid infrared range with wavelengths ranging from 5 to 50 μm are incident on a hydrogenated silicon or silicon germanium film, the photons may be directly absorbed at the band features, by phonons, free charge carriers, or impurities. In the mid-infrared region, the interaction with the sample results in rotational and vibrational transitions of the atoms or molecules. The wavelength of the absorption peak corresponds to specific chemical bond and mass of atoms. The spectral distribution of the absorption peaks of various silicon-hydrogen and germanium bonding modes has been identified by Brodsky [47], Shanks [48], and Cardona [12]. Fig. 3.7 depicts some typical bonding configurations in a-Si:H . These configurations can be roughly categorized into three modes: (1) the Si-H and SiH_2 stretching mode (2000-2100 cm^{-1}), (2) the SiH_2 and SiH_3 bond bending scissors mode (840-890 cm^{-1}), and (3) the Si-H wagging mode (640 cm^{-1}). Correspondingly, the a-(Si,Ge):H has similar bonding configurations but with different wavenumber.

The most common method of calculating hydrogen content has been proposed by Brodsky, Cardona and Cuomo(BCC) [47]. Double-side polished Si substrates were used for original IR study. This is to prevent diffuse reflection from the backside of the substrate. The equation used to calculate the hydrogen content was proposed by Cardona

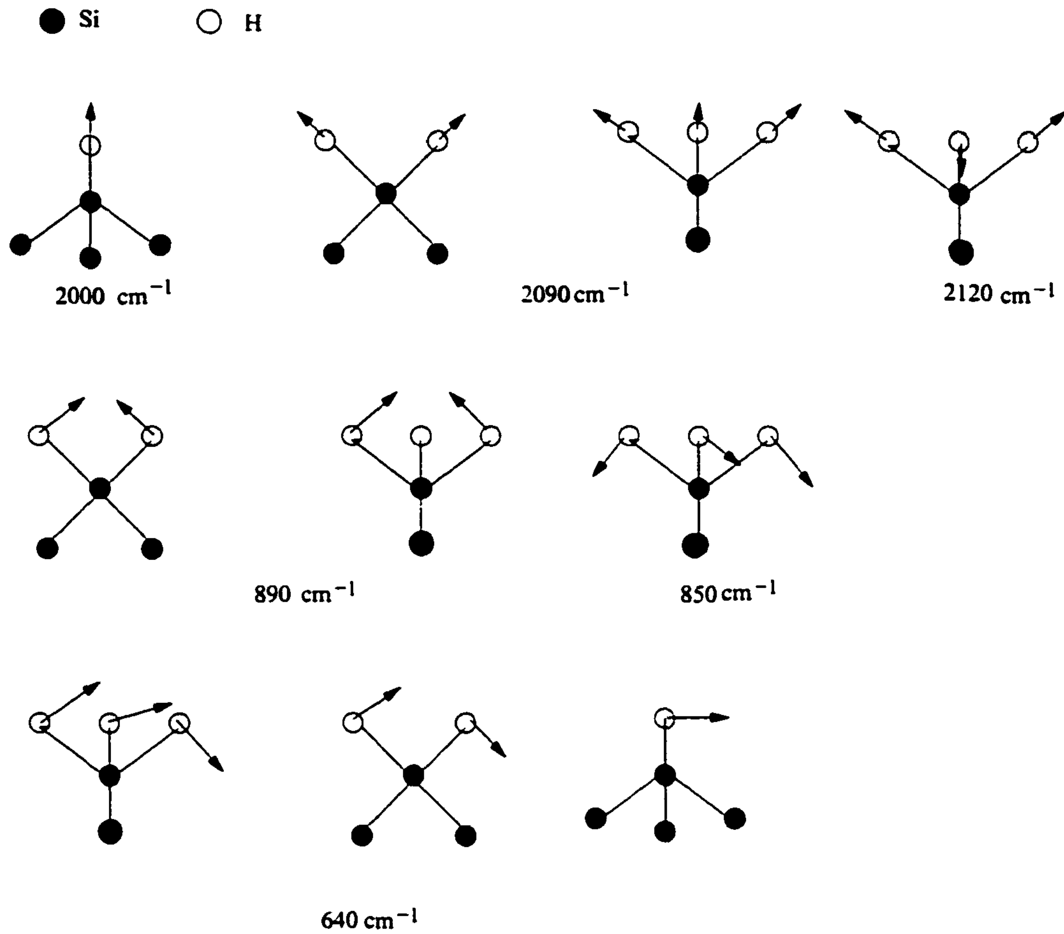

Figure 3.7 Schematic illustration of the bond-stretching(top row), bond-bending(middle row), and bond wagging (bottom row) modes of SiH, SiH_2 and SiH_3 grouping either in hydrogenated a-Si:H or gaseous silane

and later modified by Lanford [49], Maley, and Szafranek [50] :

$$N_H = A \int \frac{\alpha(\omega)}{\omega} d\omega \tag{3.12}$$

where A is an experimentally determined constant, and $\alpha(\omega)$ was the absorption coefficient at angular frequency ω. The values of A for some of the vibrational modes in Si and Ge are listed in Table 3.1.

Langford and Mayley found that, for a-Si:H , the hydrogen content determined by conventional methods from the 630 cm^{-1} absorption peak is overestimated if the film

Table 3.1 Parameter A which relates the strength of the infrared bands of a-Si:H and a-Ge:H to the hydrogen concentration

a-Si:H	$640cm^{-1}$	$840-890cm^{-1}$	$2000cm^{-1}$	$2100cm^{-1}$	$2100cm^{-1}$
Mode	Wag	Bending	Stretch	stretch	Stretch
Bonding	SiH SiH_2 SiH_3	SiH_2 SiH_3	SiH (Isolated)	SiH (Clustered)	SiH_2 SiH_3
$A(10^{19}cm^{-1})$	1.6	20	2.2	17	9.1
a-Ge:H	$565cm^{-1}$		$1895cm^{-1}$	$1970cm^{-1}$	
Mode	Wag		Stretch	Stretch	
Bonding	GeH GeH_2		GeH	GeH - GeH_2	
$A(10^{19}cm^{-1})$	1.1		≈ 5	≈ 14	

thickness is less than abut 1 μm. For greater accuracy, IR data should be analyzed by taking the effects of optical interference into account. In this project, a simple but very effective method is developed to get rid of the thickness interference. This will be discussed in the next chapter. For a-(Si,Ge):H , we could see from Table 3.1 that the Ge-H (clustered) stretching mode overlaps the Si-H (isolated) mode, thus it is not possible to get the hydrogen content by integration over the 2000 cm^{-1} range. The conventional and most common used mode to calculate the hydrogen content is the wagging mode. For this research, the IR data were taken by a Nicolet 510 Fourier transform infrared spectrometer, with a mid-IR detector using Omnic spectroscopy software.

3.2 Device characterization methods

The ultimate goal of this research is to make high performance a-(Si,Ge):H solar cell devices. The performance of a solar cell can be characterized by its I-V curve, quantum efficiency and fill factor. Other techniques such as thickness, hole lifetime ($\mu\tau$) product, Urbach energy and midgap defect density are also useful characterization tools to understand the physics of the device.

3.2.1 I-V curve

The performance of a solar cell under illumination can be described by current voltage dependence. A typical current-voltage curve of a p-i-n solar cell under illumination is shown in Fig. 3.8. We can define three parameters that give a rather complete description of the electrical behavior. These three parameters are usually quoted in literature to determine a device is good or not. And, we can define the parameters in terms of the circuit model components. The equivalent circuit is already shown in Fig. 2.3.2. From

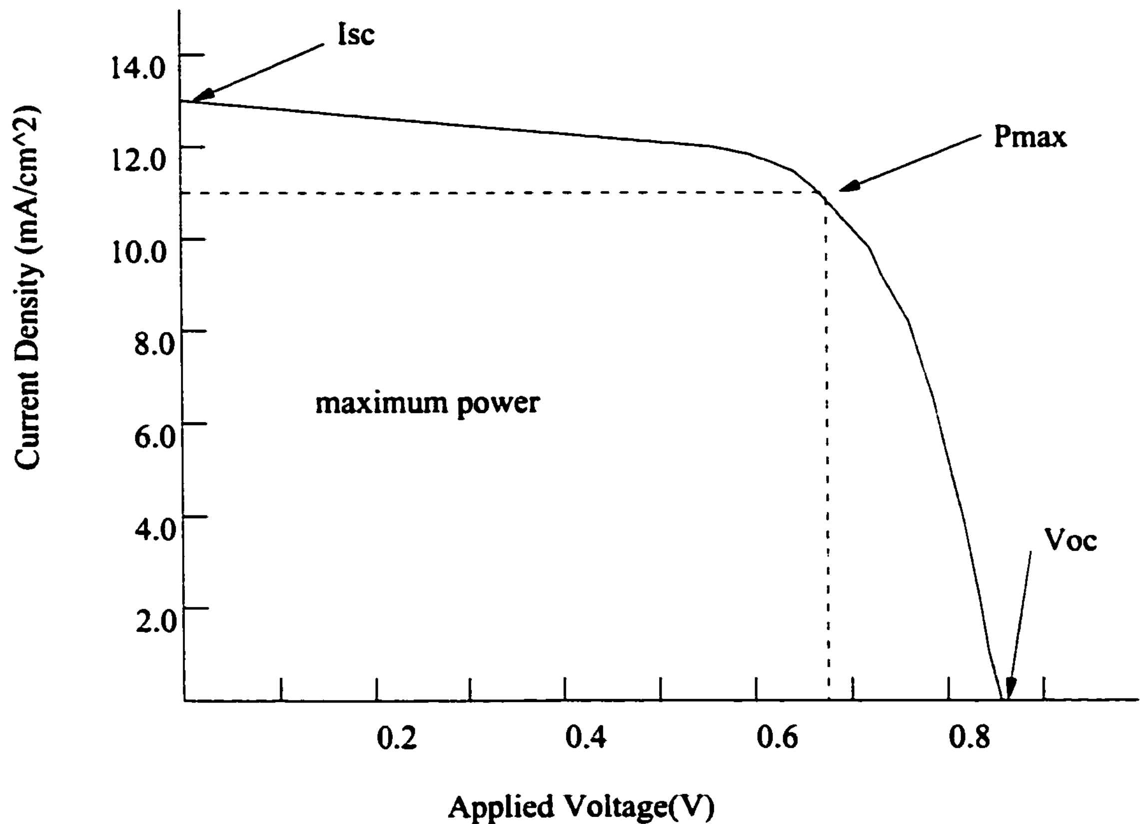

Figure 3.8 Current voltage characteristics of an illuminated p-i-n diode

the equivalent circuit, the current-voltage characteristics of the device are given by

$$J(V) = J_s[e^{\frac{qV}{AkT}} - 1] - J_L(V), \tag{3.13}$$

where J(V) is the current density at applied voltage V, J_s is the saturation current, A is the diode factor, k the Boltzmann constant, T the temperature and J_L the photo generated current density.

The first parameter is the short circuit current J_{sc}, which is the current of the cell under illumination for V=0. From equation 3.13, it is equal to $J_L(0)$. The photo-generated current, also called the short-circuit current, depends upon the spectrum of the incident light, the material response to the light and the collection efficiency. Thus it can be rewritten as

$$J_L = q\int(1-R)Q(E)S(E)dE, \tag{3.14}$$

where R is the reflection coefficient, S(E) the spectrum of the light source and Q(E) the collection efficiency of the structure.

The second parameter is the open-circuit voltage V_{oc}, which is obtained for J(V)=0. Thus from equation 3.13 we get

$$V_{oc} = \frac{AkT}{q}\ln[\frac{J_L}{J_s}+1]. \tag{3.15}$$

For a diode junction, the saturation current can be expressed as [51]

$$J_s \approx \frac{qn_iW_d}{2\tau}, \tag{3.16}$$

where

$$n_i = \sqrt{N_C N_V}\exp(\frac{-E_g}{2kT}), \tag{3.17}$$

so that

$$V_{oc} \approx \frac{kT}{q}\ln(\frac{J_L}{J_s}) \approx \frac{kT}{q}[\ln(J_L) - \ln(\frac{qW_d}{2\tau}\sqrt{N_C\cdot N_V})] + \frac{E_g}{2q}. \tag{3.18}$$

Here, n_i is the intrinsic carrier density, E_g the band gap, W_d the depletion width of the junction. We can see that E_g is the dominant factor in the expression for the open-circuit voltage, while the lifetime and thickness affect the open-circuit voltage as well.

The performance of the solar cell is eventually determined by the fraction of the total power of incident light can be converted into electrical power. In general, the solar cell

will be operated under conditions that give maximum power output. The maximum possible area in Fig. 3.8 for a given current voltage curve determines the fill factor FF, which is defined by

$$FF = \frac{V_m I_m}{I_{sc} V_{oc}}$$

The more "square-like" the current-voltage curve is, the larger the FF. The fill factor provides an indication of the quality of the material used in the i-layer, and how well the solar cell is designed. A high fill factor requires low loss of photogenerated carriers in the i layer (i.e. large mobility life-time product $\mu\tau$) and interfaces, strong electric field in the i layer, and good ohmic contact. High-quality a-Si:H cells with good design have fill factors of about 66% to 70% with open-circuit voltage around 0.84 V. For a-(Si,Ge):H devices with straight band gaps, the fill factor is up to 65% for the best devices at a band gap of 1.5 eV.

The three parameters V_{oc}, J_{sc}, and FF are sufficient to calculate the energy-conversion efficiency η of the solar cell. It is definсd by the ratio of maximum power that is extracted from the cell to the total illumination power. It is represented by the following equation,

$$\eta = \frac{FF \cdot V_{oc} \cdot I_{sc}}{\phi_{in}}. \tag{3.19}$$

where ϕ_{in} is the total incident power of the photons. In this project, the area of the cells is around 0.08 cm^2, the light source used for I-V measurement is an ELH lamp operating at 115V, 2.4 A.

3.2.2 Quantum efficiency

The quantum efficiency (QE) measurement is another useful diagnostic tool to characterize the performance of solar cell devices. Quantum efficiency is defined as the ratio of the number of charge carriers collected to the number of photons incident on the sample at a particular wavelength. QE measurements provide information on how well the device absorbs photons at various wavelengths, and how well the photo-generated

carriers are collected under normal forward-bias operating conditions. The internal electric field is reduced with biasing in the forward direction, and the QE results provide details as to how this reduction affects the collection of photo-generated carriers. Also, any problems in the device design that may inhibit collection of excess carriers, such as hole trapping at the p-i interface, can be uncovered. Finally, the dependence of the QE at a particular wavelength, on the bias voltage can be used to estimate the material transport parameters.

The collection efficiency peaks at about 80-90% for wavelengths between 500-600 nm. However, for a-SiGe:H, the lower band gap extends the spectrum to longer wavelengths than a-Si:H . The decreasing collection efficiency at shorter wavelengths can be attributed to several effects. One is the absorption of light in the p layer that is directly exposed to the incident light. The resulting photo-excited carriers give little contribution to the charge collection because of the low minority carrier lifetime in the doped material. Another cause is the back diffusion of the excess electrons generated close the p layer. Some electrons with high energy could overcome the barrier of the p-i junction. These back-diffused electrons recombine with holes and reduce the current. The drop off at the longer wavelength is due to the smaller absorption coefficient.

QE measured at zero bias provides important information about the cell. We can have an idea about the thickness of the i layer by looking at the QE values at short wavelengths. Too thick an i layer would lead to a very low QE value and too thin would result in unreasonably high QE. For a thick i layer, the hole has to travel longer before it can be collected by the p layer. This increases the chance of recombination during the transport. Also, the interface between the p and i layers has impact on the short-wavelength QE. A badly designed buffer layer or defective buffer could reduce the QE. QE values at long wavelengths tell us about the collection efficiency for low-energy photons. It is also affected by the quality of the i layer. Photo-generated minority carriers in the bulk will be trapped by a defective i layer before they can be collected by

the p^+ layer.

The QE measured under bias can tell us about the electric field profile inside the cell. When the solar cell is under forward bias, the internal field is reduced. As a result, the collection efficiency is reduced since the carrier collection of solar cell relies on the assistance of the electric field. For high-quality solar cells, the mobility-lifetime product of the minority carriers is so large that that a small forward bias applied to the cell will not affect the carrier transport to a great extent. Thus the ratio of the QE under forward/reverse bias and zero bias can provide information how strong the internal electric field is and how large $\mu\tau E$ is. This issue will be further discussed in the next section. Fig. 3.9 shows the quantum efficiency curve with and without bias, and the QE ratio. The quantum efficiency is a relative value. We assume that the peak value of the quantum efficiency in the range of we are interested in is 0.9 and any other values are normalized to this peak value. The absolute value of the quantum efficiency could be obtained by carefully calibrating incident photons and calculating the exposed area. A TCO contact is also required.

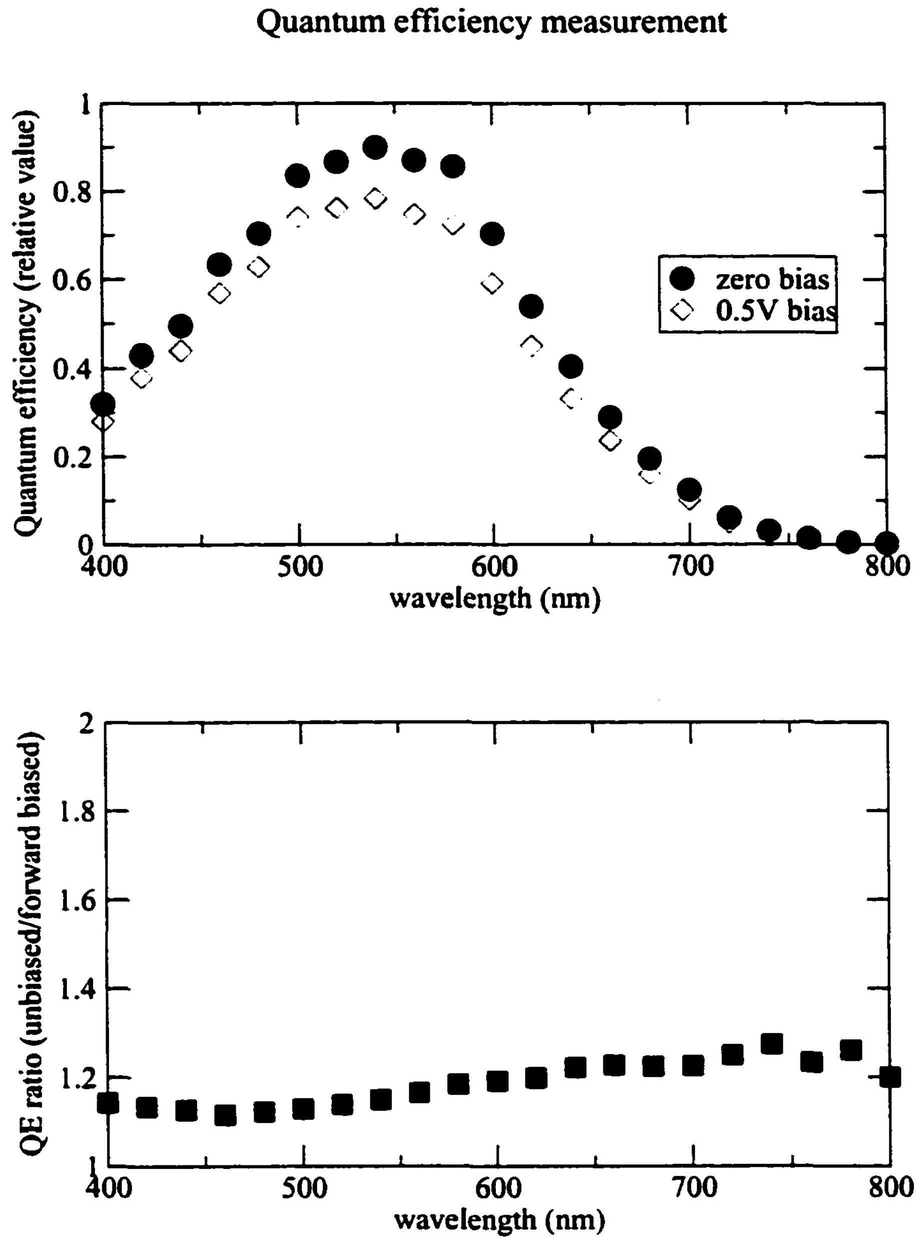

Figure 3.9 Quantum efficiency curve and quantum efficiency ratio curve

3.2.3 Hole $\mu\tau$ product

The $\mu\tau$ product of holes is a very important parameter for devices. It is the quantity which primarily determines the fill factor and the behavior of the QE ratio of the cell. Large $\mu\tau$ means that the holes can drift longer with the assistance of the internal field and be collected by the p layer before they are trapped and recombine. Therefore, in order to have a high collection efficiency, the hole range, $\mu\tau$E, must be large compared to thickness of the i-layer. In a-Si:H solar cells, this condition is easily met; however, in a-(Si,Ge):H devices, especially fabricated with a high growth rate, the higher defective density severely reduces both the electric field and $\mu\tau$ product. This results in lower collection efficiency, particularly under forward bias conditions.

The quantum efficiency measurement gives a convenient way to estimate the $\mu\tau$ product. The QE can be expressed as

$$QE(\lambda, V) = \int_0^t \alpha(\lambda) \cdot e^{-\alpha x} \cdot e^{-\int_0^x \frac{1}{L_d(V)}} dx, \tag{3.20}$$

while

$$L_d(V) = \mu\tau E(V).$$

The QE value can be obtained by measurement, but the electric field has to be found in another way. The simplest way is to assume that the electric field in the bulk is constant so that it is determined by $E = V/d$ [52]. This assumption works well for estimation. In real devices, due to the high defect density near the interface, the electric field is not constant. The AMPS-1D program developed by Penn State University can simulate the profile of the electric field. It shows that the electric field is high near the interface and drops down quickly in the middle, but this involves complicated models. Dalal and Haroon [53] simplified the model by assuming that the charge density drops down exponentially from both interface and it is symmetric. Poisson's equation gives

$$\frac{dE(x)}{dx} = \frac{\rho(x)}{\epsilon_s},$$

where $E(x)$ is the electric field and $\rho(x)$ the charge density and ϵ_s the permitivity of the material. As in Dalal's model,

$$\rho(x) = q \cdot N_o \cdot exp(ax),$$

where N_0 is chosen such that the total charge density $N_t = \int exp(ax)dx$ is compatible with our space charge limited current measurement(SCLC). We can get

$$E(x) = \frac{q \cdot N_0}{\varepsilon_s \cdot a} exp(ax) + \varepsilon_0,$$

where

$$E_0 = (V_{bi} - V_{app} - \int_o^{W_d} \frac{q \cdot N_0}{\varepsilon_s \cdot a} \cdot e^{ax} dx) \cdot \frac{1}{L}.$$

Since we know the electric field, it is not difficult to get $\mu\tau$. The basic idea is quite simple. We measure the quantum efficiency of the device for several wavelengths, as a function of applied voltage. The QE increases under reverse bias and decreases under forward bias. If we assume that $\mu\tau$ does not change with bias voltage or wavelength, the QE variation solely comes from the change of the electric field profile. All of these curves should have the same $\mu\tau$ value. By modeling the electric field and substituting the $\mu\tau$ value into equation 3.20 with the trial and error method, we could get another group of curves which should match the experimental curves very well. In experiments, we choose the QE in the long wavelength range where the generated carriers are not affected by the defective interface states and back diffusion. Fig. 3.10 shows an experimental result with a simulated result.

3.2.4 Space-Charge-Limited Current (SCLC)

A classical technique used to study the electronic density of states (DOS) continuously distributed in the gap of insulating thin-film materials is the measurement of the space-charge-limited currents (SCLC) [54, 55]. In this experiment, voltage applied

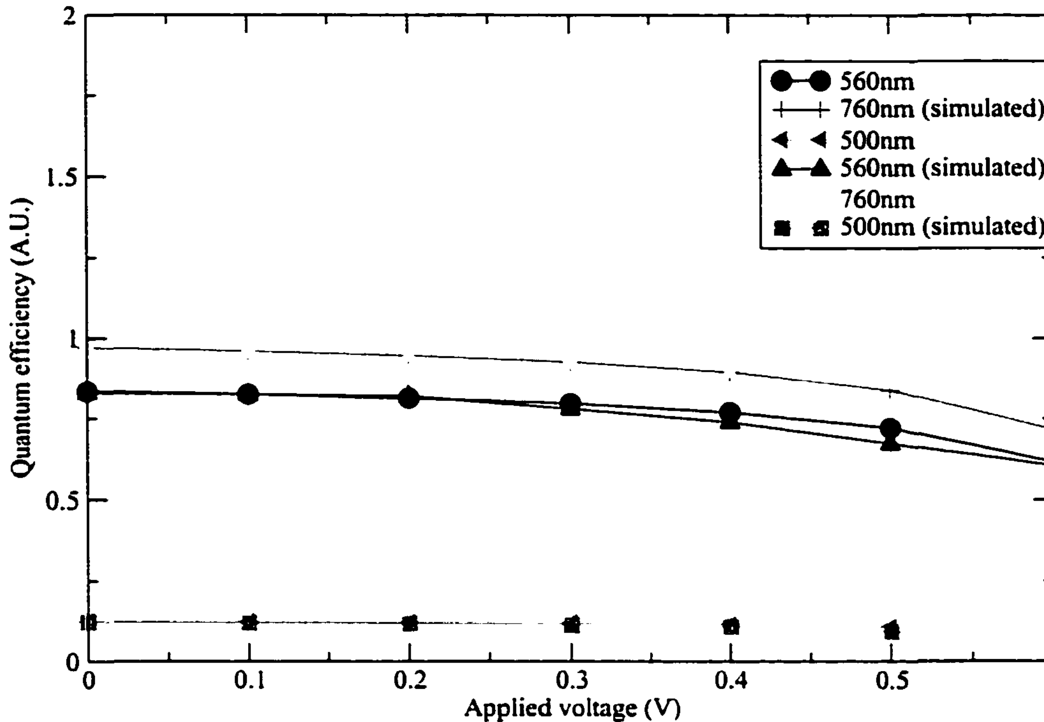

Figure 3.10 A simulation result of quantum efficiency against the experimental result

across a thin diode causes an electrode (the "cathode") to inject a non-equilibrium density of electronic charge, which populates the empty gap states above the Fermi level E_F in the vicinity of the cathode. When the applied voltage is large enough, this extra charge extends across the entire sample thickness, and the current collected by the counter electrode (the "anode") becomes space-charge-limited. Almost all the charge is trapped, but an exponentially small fraction is thermally promoted to the conduction band edge E_c, increasing the current measured. It is this bulk enhancement mechanism which is analyzed to provide information about the density of the electronic states above the equilibrium Fermi level. For the states under the Fermi level, a $p^+ - i - p^+$ structure

is used to suppress the electrons so that only holes are injected into the bulk. A typical I-V curve of the SCLC measurement is shown in Fig. 3.11.

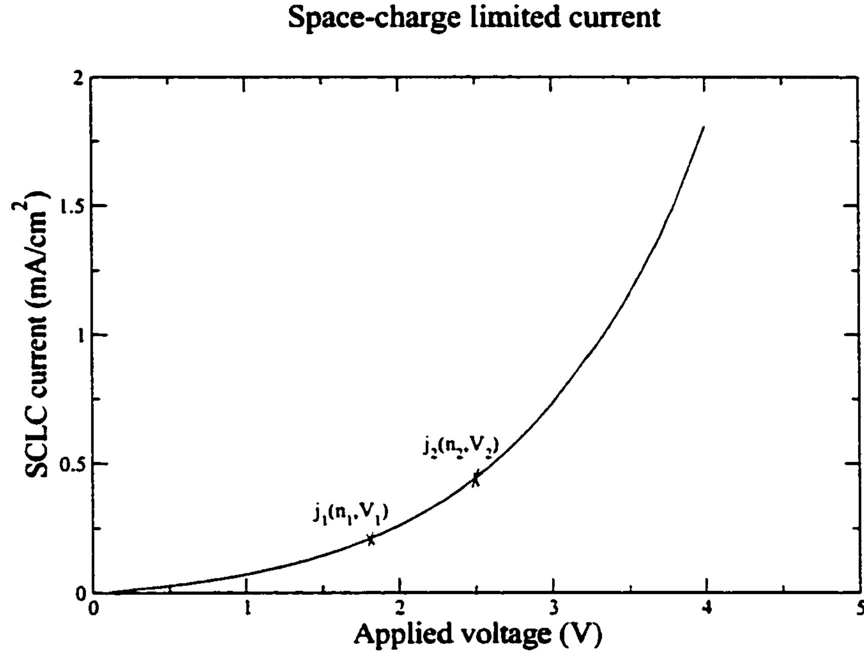

Figure 3.11 plot of current density J against applied voltage for a symmetric $n^+ - i - n^+$ specimen at room temperature.

The theory behind the measurement was developed by many authors [54, 55, 56]. Ohm's law says

$$j_1 = n_1 e \mu_n V_1 / L, \quad (3.21)$$

$$j_2 = n_2 e \mu_n V_2 / L, \quad (3.22)$$

where j_1 and j_2 are the current density values shown oi Fig. 3.11. n_1 and n_2 are the conduction band carrier densities

$$n_i = N_c \exp(-\frac{E_C - E_{Fi}}{kT}), \quad (3.23)$$

and E_{Fi} is the quasi-Fermi level moved by the injected carriers. Assume that the injected charge is uniformly distributed across the film, the electric field is constant and equal

to V/L throughout the film. Another assumption is that that the trap distribution $N_t(E)$ is continuous and only slowly varying. Therefore, the trap density of states can be approximated as

$$n_t - n_{t0} \approx \int_{EFo}^{E_{Fn}} N_t(E)dE, \tag{3.24}$$

and Poisson's equation gives

$$eL(n_t - n_{t0}) = \frac{2\varepsilon_s V}{L}. \tag{3.25}$$

Then, from 3.21, 3.22 and 3.23, we get

$$\Delta E_F = E_{F2} - E_{F1} = kT \ln \frac{n_2}{n_1} = kT \ln \frac{j_2 V_1}{j_1 V_2}. \tag{3.26}$$

We then can rewrite Equation 3.25 as

$$\frac{2\varepsilon_s \Delta V}{L} = eL \int_{E_{F1}}^{E_{F2}} \widetilde{N_t}(E)dE. \tag{3.27}$$

The integral in 3.27 can be approximated by

$$\int_{E_{F1}}^{E_{F2}} \widetilde{N_t}(E)dE \approx \widetilde{N_t} \cdot \Delta E_F, \tag{3.28}$$

where $\widetilde{N_t}$ is the average trap density between E_{F1} and E_{F2}. Finally, we get

$$\widetilde{N_t} \approx \frac{2\varepsilon_s \Delta V}{eL^2 \Delta E_F}. \tag{3.29}$$

Since $\widetilde{N_t}$ is the density at a certain energy level, by differentiating the J-V curve, we could get the density at different energy levels. Fig. 3.12 shows the density map of a sample.

In this study, the thickness of the sample is more than 1 μm so that the density of interfaces is ignorable . The measurement is taken in a black box at elevated temperature to eliminate the photo-generated current and overcome the Shockley barrier.

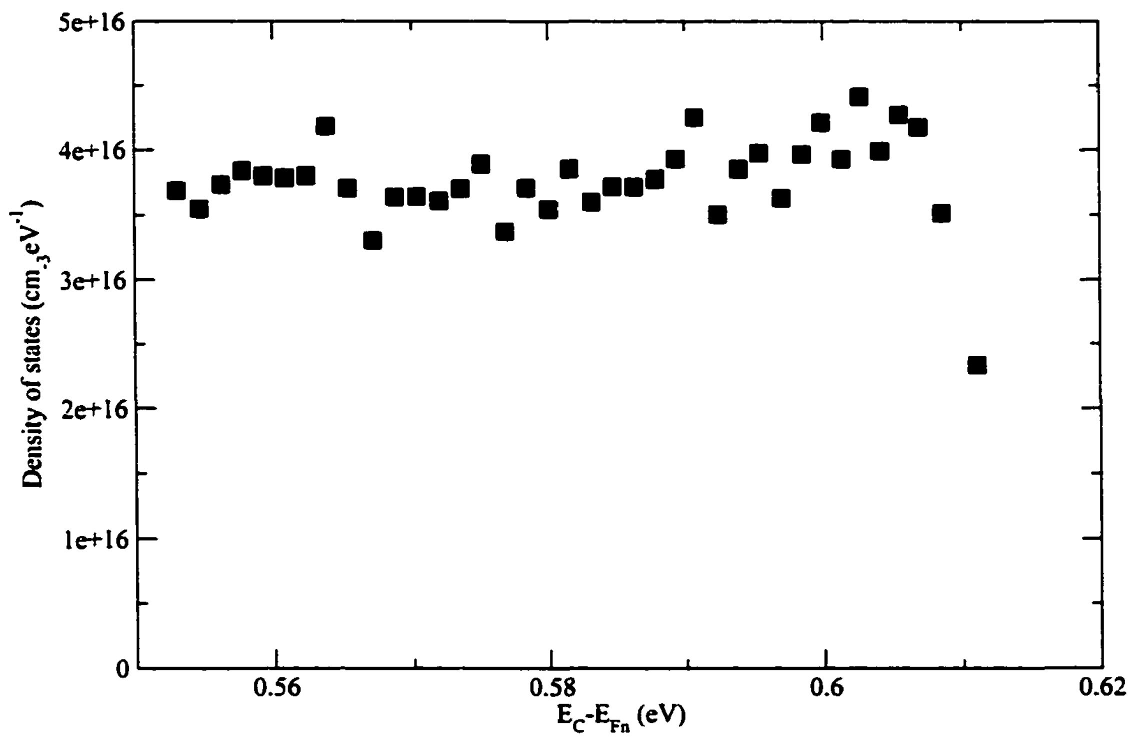

Figure 3.12 Density of states calculated by differential method

CHAPTER 4. RESULTS AND DISCUSSION

4.1 The SCLC measurement results

It is mentioned in chapter 3 that Fourier-Transform Infrared (FTIR) spectroscopy is an effective diagnostic tool to analysize the microstructure and hydrogen bonding in amorphous silicon and amorphous silicon germanium materials. It was intensively used in this project. Several series of hydrogenated amorphous silicon germanium films have been deposited by the ECR PECVD technique onto double-side polished crystalline silicon substrates. Hydrogen bonding and hydrogen content were examined. Silane and 20% Germane (diluted in H_2) were used as the deposition gases. PPM TMB was introduced during the deposition to compensate the contamination of oxygen from the glass window of the reactor. The plasma species were hydrogen and helium ions, respectively. The selection of the deposition parameters was based on the design of experiments. For example, in order to investigate the ion flux effect, all the parameters ware kept as constant as possible except the pressure, and then another series of samples were deposited with another set of parameters to make sure the results are only pertain to the ion-flux effect. Table 4.1 shows the deposition parameters of the samples that FTIR measurements were performed on.

The 510 Nicolet Fourier-transform infrared (FTIR) spectrometer, with a detector operated at a resolution of 4 cm^{-1} resolution was used. For this spectrometer, the absorptance spectra were first obtained using Omnic spectroscopy software. 10000 scans were typically averaged to get a high signal to noise ratio. Each spectrum was corrected

Table 4.1 Substrate deposition pressure, film thickness, Hydrogen content vs ECR-PECVD film sample number

Sample number	Pres mTorr	H_2	He	$\frac{SiH4}{GeH4}$	$L(\mu m)$	C_H (at %)	FWHM (2000)	$\frac{1890}{2000}$	v(640)	v(2100)
5277	5	60	0	2.5	1.47	3.9	94	0.15	630	N
5278	5	60	0	1.25	2.25	4.5	107	.45	620	N
5279	5	60	0	0.83	2.74	4.25	98	.8	610	N
5280	15	60	0	2.5	1.1	3.8	90	.183	630	Y
5281	15	60	0	1.25	1.5	3.2	85	.78	600	Y
5282	15	60	0	0.83	1.82	1.75	91	1.78	590	Y
5283	7	100	0	0.83	2.1	3.85	103	.63	613	N
5284	15	100	0	0.83	1.7	2.25	87	1.36	590	Y
5285	5	75	0	0.83	1.45	3.52	100	0.67	620	N
5286	20	100	0	0.83	...	...	...	...	...	...
5287	10	10	50	1.25	1.64	4.3	107	0.35	620	N
5288	10	10	50	0.83	2.47	3.5	94	0.64	615	N
5291	20	10	50	0.83	...	...	...	...	...	N
5293	10	10	50	2.5	2.18	6.5	100	0.2	633	N
5294	35	10	50	0.83	...	...	...	...	...	Y

for H_2O and CO_2 artifacts using previously generated reference spectra, followed by a manual baseline correction to remove the sinusoidal fringes. The sinusoidal fringes were caused by the interference of finite thickness of the film. Since the permitivity of amorphous silicon germanium changes with frequency, the sinusoidal frequency and the magnitude are not constant. Instead, it changes considerably in the range from 400 to 2500 cm^{-1}. An empirical model for the magnitude of the baseline ($y(\omega)$) was developed,

$$\begin{aligned} y(\omega) &= A(\omega)\sin(k(\omega)\cdot\omega+\phi_0)+y_0, \\ A(\omega) &= A_0(1+k_1\omega), \\ k(\omega) &= k_0(1+k_2\omega), \end{aligned}$$

where $A(\omega)$ is the amplitude of the "sinusoidal wave", k the period constant which is close to πt, t is the thickness of the film. We assume that $A(\omega)$ and $k(\omega)$ have linear relations with wavenumber (ω), which is quite accurate for this purpose. The trial and error method was used with Matlab to determine constants such as k_0, k_1 and Y_0. In

order to get precise values for these constants, the film can not be too thin. Otherwise, there will not be enough peaks to roughly determine the constants and fine tune the equations. Fig. 4.1 shows the spectra before and after the baseline subtraction.

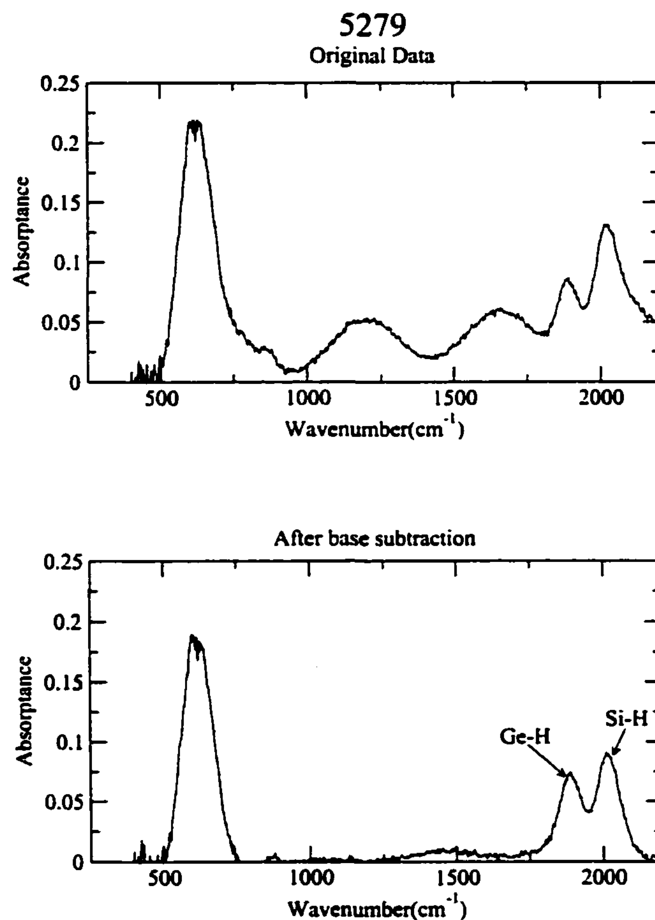

Figure 4.1 Illustration of baseline subtraction: The height of the characteristic peaks, as well as the width of the peaks, have been changed after the base deduction. The interference fringes are nicely removed. The original data is on the top, the bottom graph is after baseline subtraction

It has been known for a long time that the hydrogen in the amorphous Si is under-

estimated or overestimated by using Cardona's model [47] (BCC method).

$$N_t = A \times \int_{\omega^*} \frac{\alpha(\omega)}{\omega} d\omega. \tag{4.1}$$

The errors in the BCC method are primarily a function of the optical path length, i.e., the product of index and film thickness. The errors also depend on the film refractive index and absorption coefficient, although to a less extent. Langford [49] etc., modified the model by using an empirically determined correction factor,

$$\alpha = \alpha_{BCC}/1.72 - K\omega d. \tag{4.2}$$

Here, d is in μm, K=0.0011. Note that this correction is an approximation and the errors in α can still be an order of 10-20% [50]. The manual base subtraction is a little time consuming, but has higher precision. In Fig. 4.1, the Ge-H stretch peak is only one half of the Si-H peak on the raw data. However, after the baseline correction, the Ge-H peak is comparable to that of the Si-H.

From the IR spectra we calculated the absorption coefficient of the Si-H mode (640) and Ge-H mode (570). However, it is impossible to deconvolute the overlapping bands of the two peaks but integrate them together by using a corrected constant A. The proportionality constant A depends on the composition of the $a-Si_{1-x}Ge_x$. A differential method was developed by assuming that the constant A is a linear function of the composition ratio x,

$$A = A_{Si-H} \cdot (1-x) + A_{Ge-H} \cdot x \tag{4.3}$$

The integration in equation 4.1 was calculated in Matlab. The values of hydrogen content are listed in Table 4.1. The initial observation illustrates that all the values are well below 10%, which is believed to be in the range of "device quality" [1]. However, the nuances of the spectra explained the big differences in the material properties and device performance. Furthermore, it provides us a good chance to study the growth chemistry of the ECR-PECVD.

4.1.1 Ion flux effect

A lower pressure in the vacuum system results in longer mean free path, thus more hydrogen atoms are ionized. From Table 4.1, the results of two series of a-(Si,Ge):H films, one deposited under 5 mTorr and the other under 15 mTorr are given. The biggest difference between these two series are the poly-hydride peak at 2100 cm^{-1}. Fig. 4.2 shows the difference. The 5mTorr (top) films doesn't have this peak although the

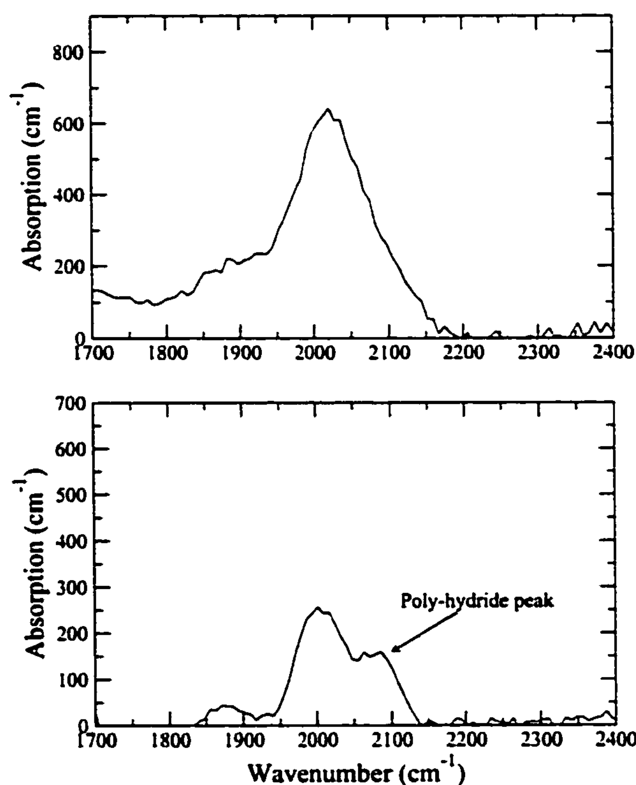

Figure 4.2 The stretch mode and poly-hydride mode of two samples grown at 15mTorr and 5mTorr respectively. The Ge-H stretch mode is not obvious due to low Ge content.

stretch peak around 2000 cm^{-1} is a little wider. The poly-hydride peak indicates that the 15 mTorr films have more microvoids and clustered hydrogen, which gives poorer

electronic properties. Zhiyang Zhou and Dalal [26] showed that the a-(Si,Ge):H films and devices grown at low pressure in a pure hydrogen plasma have better quality. Optical and electronic properties, including band gap, Urbach energy and mobility-lifetime for both electrons and holes were found to be greatly improved at low pressure. In Table 4.1, the band gap change due to the variation of pressure is indicated by the shift of the wag mode peak (around 640 cm^{-1}). The peaks of low-pressure samples are slightly shifted by 10-20 cm^{-1} toward higher frequency, this means they have higher band gap. One possible reason is that ions from low pressure have more energy and break the Si-H bond easily so that more Si is incorporated. Comparing the two spectra, we can find that the amplitude of the stretch mode (Si-H bond) for the low-pressure sample is much higher than that of the higher-pressure sample. This surprising result also tells us that the stretch mode (Si-H and Ge-H) is predominant in the materials grown under optimal plasma conditions while the higher pressure samples have more microstructures.

4.1.2 He plasma

The initial observation which best illustrates the difference in the He plasma (high growth rate) films, compared to those of normal (15 mTorr) a-(Si,Ge):H films is also shown in Table 4.1 and summarized in the following:

1. All the spectra from the He plasma films do not have the 2100 cm^{-1} peak except the very high pressure one (35mTorr). It gives a conclusion that the amount of microstructure is largely removed. The FWHM at 2000 cm^{-1} is close to the 5mTorr H_2 samples'.

2. The other noticeable difference is the peak value of wag mode. For the same GeH_4/SiH_4 flow ratio, the He plasma samples have the highest value, which means the band gaps are higher than that of pure hydrogen dilution plasma samples.

3. The hydrogen content decreases with increasing of GeH_4/SiH_4 ratio. This is understandable. The Ge-H bond is weaker than the Si-H bond. It has a larger probability

of forming a dangling bond, Ge-. The more Ge coming into the alloy, the more dangling bonds (Ge-H), and the lower the hydrogen content. This is different from the hydrogen dilution film. In that case, there is more than enough hydrogen ion flux, so that the dangling bonds get a lot more chances to capture atomic hydrogen and are passivated. However, if the pressure is too high (e.g., 15 mTorr) , even if there is more than enough H_2, the hydrogen ion flux is insufficient due to the low ionization ratio, which will leave a lot of dangling bonds. The H content difference in sample 5279 and 5282 supports this conclusion.

4. Surprisingly, the H content in the helium films as large as the best hydrogen films. For some time, people believed that the heavier ion bombardment of helium ions removed a lot of hydrogen from the surface and left a lot of dangling bonds in the bulk. And this case became worse when germanium was incorporated into the alloy, since the Ge-H bond is weaker than the Si-H bond. Our results imply that with the ECR-PECVD technique, we could get a high growth rate without compromising the quality of the material.

4.1.3 Discussion about the growth chemistry

We roughly discussed the growth model in chapter 2 without supportive experimental results. As has been mentioned, the hydrogen plays an important role in the growth chemistry. It enhances the radical selectivity by increasing the fraction of silyl radicals in the growth chemistry,

$$H + SiH_2 \longleftrightarrow SiH_3, \tag{4.4}$$

$$H + SiH \longleftrightarrow SiH_2. \tag{4.5}$$

It partially explains why the higher pressure hydrogen dilution films have more microvoids and poorer properties, because there are more than one kind of radical resulting in inhomogeneous growth. The hydrogen ions also remove hydrogen from the surface

and subsurface. H-ions with enough energy can penetrate into the lattice to improve the microstructure by removing the weakly bonded H and reconstruct the subsurface structure. This is the biggest difference between the H dilution and He dilution. The helium dilution plasma could also remove the H from the surface by breaking the Si-H bonds since it has higher energy and is heavier. However, He is considerably bigger than H and cannot penetrate the surface. Fig. 4.3 are the spectra of sample 5277 and 5293. These two samples have the same GeH_4/SiH_4 flow ratio but in a different plasma. From this figure, we can see that they have almost the same amount of Si-H (stretch mode) bond, but 5293 has more H than 5277. One possible reason is that there is not enough hydrogen in the He plasma. The film did not benefit from the subsurface H reconstruction. With a higher GeH_4/SiH_4 ratio, this film quality improved a lot, since the Germane (GeH_4) itself is diluted in hydrogen gas (We used 20% GeH_4 gas). More GeH_4 flow ratio will also bring in more H_2. Table 4.1 reflects the change: The H content in samples 5287 and 5288 drops to the same level as these of samples 5277 and 5278. The hydrogen dilution effect will be further verified in later experiments.

One of the advantages of inert ions is the bombardment. The quality of a-SiGe:H depends on how uniformly the germanium is incorporated into the alloy. The radical germyl is very heavy. For low temperature epitaxy growth (200-350 ^oC), the surface mobility is very low. This will give rise to clustered and columnar epitaxy growth and degrade the material. The ion bombardment can promote the diffusion of germyl radicals on the surface. At the same time, this bombardment helps to break the Si-H or Ge-H bond so that the Ge and Si atoms are cross-linked. Thus a uniform growth is achieved. The absence of a SiH_2 peak in the spectra of He films also proved that He ions are very effective at removing the excess H and improve the material quality. Actually, a high-energy H flux can also achieve this aim. In contrast, a high pressure discharge does not provide enough H ion flux, and the germyl radical does not diffuse readily, giving rise to a film with Ge clusters and poorer properties.

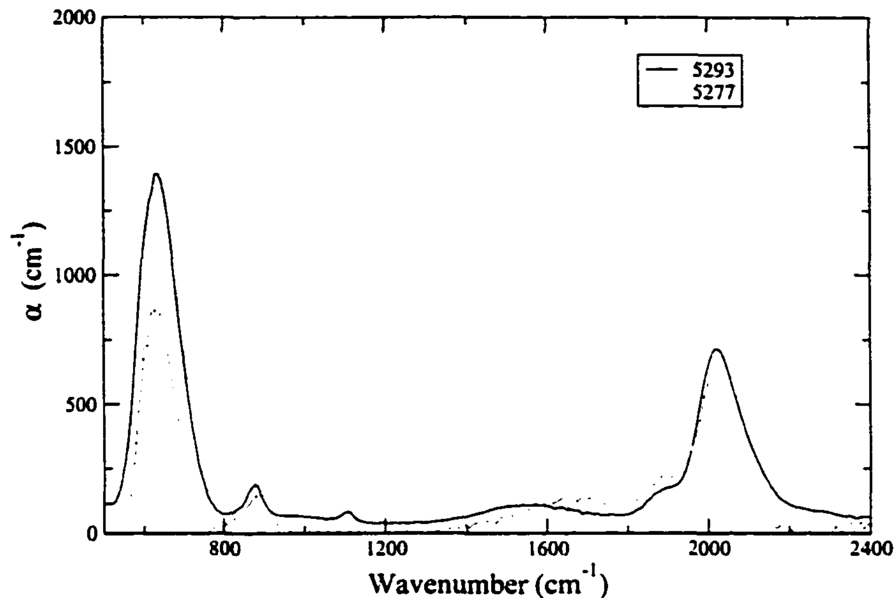

Figure 4.3 The spectra of 5277 and 5293. Since the GeH_4/SiH_4 flow ratio is small, the 1890cm^{-1} Ge-H peak is not prominent. If take into account the baseline mismatch of the two curves, we could see that the two spectra overlap around 2000 cm^{-1}

One of the concerns about the high-growth-rate deposition of a-(Si,Ge):H film is that the preferential H-bonding to Si is too large, so that there will be a lot of Ge- dangling bonds. This is because the Ge-H bonds are weaker than the Si-H bonds and the heavy inert ions can easily break them. These dangling bonds will behave like excess carrier traps and severely degrade the lifetime the carriers. It is well known that in PECVD-grown a-SiGe:H, H bonds preferentially to Si by a factor of at least five [58], while in high-growth-rate condition, the factor seems to be as large as ten [59]. Therefore, we can barely see the 1890cm^{-1} Ge-H peak but only the 2000cm^{-1} Si-H peak. In our films, the preferential factor is around two to three, which is much better than the other groups' results. Fig. 4.4 shows the stretch peaks of a-(Si,Ge):H , where the Ge-H is obvious.

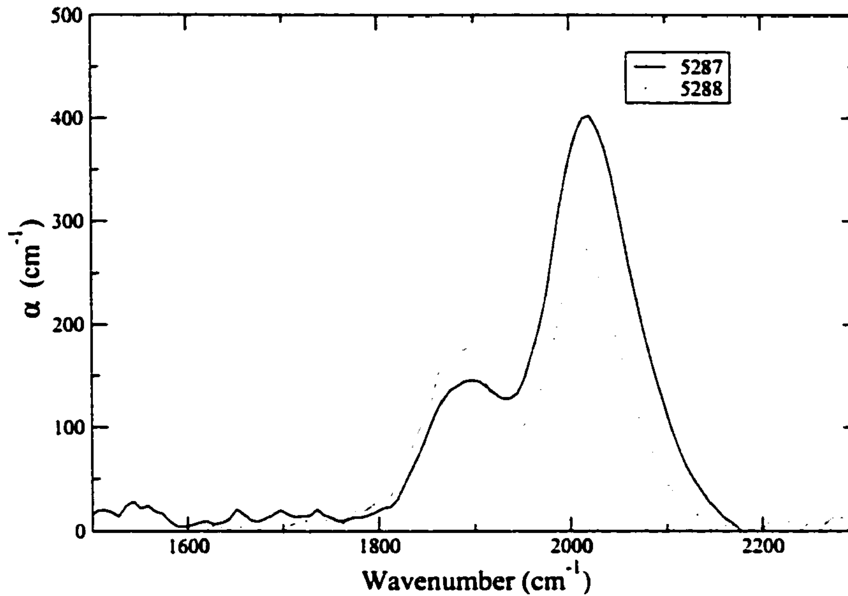

Figure 4.4 FTIR spectrum of a-(Si,Ge):H films grown at high growth rate conditions, clearly showing the Ge-H peak around $1890cm^{-1}$ and the Si-H peak around $2000cm^{-1}$. The prefactor can roughly be determined by the height of the peak.

4.2 General characteristics of a-(Si,Ge):H grown under high growth rate condition

The FTIR results give us confidence that a-(Si,Ge):H films deposited with a high growth rate are as good as, if not better than, the normal-growth-rate films. In order to characterize the optical and electrical properties of the material, films were deposited on Corning 7059 glass substrates. Various growth conditions such as pressure, hydrogen dilution, substrate bias, and microwave power have been investigated to find the optimal parameters. Conductivity, band gap, subgap absorption and mobility-lifetime were systematically measured on these samples.

4.2.1 The effect of pressure

The pressure affects the mean free path of the electrons and ions which eventually affect the ionization ratio, ion flux and the energy of ions. As has been mentioned in previous chapters, low pressure can generate more ions.

Two series of samples were made to study the impact of pressure on the materials. The parameters are listed in Table 4.2.

Table 4.2 Deposition parameters for pressure investigation

Sample	Temperature ^oC	Pressure mTorr	Power	H_2 %	He %	SiH_4 %	GeH_4 %	TMB %
2/5496	300	10	150W	10	50	10	20	10
2/5491	300	15	150W	10	50	10	20	10
2/5492	300	20	150W	10	50	10	20	10
2/5493	300	25	150W	10	50	10	20	10
2/5521	300	10	150W	10	50	10	40	10
2/5495	300	15	150W	10	50	10	40	10
2/5519	300	20	150W	10	50	10	40	10
2/5520	300	25	150W	10	50	10	40	10

Photoconductivity, subgap absorption as well as the $\mu\tau$ product were measured. The results are shown in Fig. 4.5

For this particular set of parameters, 15 mTorr is better than the other pressures. With higher pressure, there is not enough ion flux or enough ion bombardment, as has been discussed earlier, and the films' properties are poorer. However, the 10 mTorr samples are not good either. This issue will be discussed later.

The calculation of $\mu\tau$ is based on the measurement of photoconductivity; however, the conductivity under AMS 1.5 is not an accurate method to fulfil this purpose. Therefore, a precise $\mu\tau$ measurement is performed and described in the following.

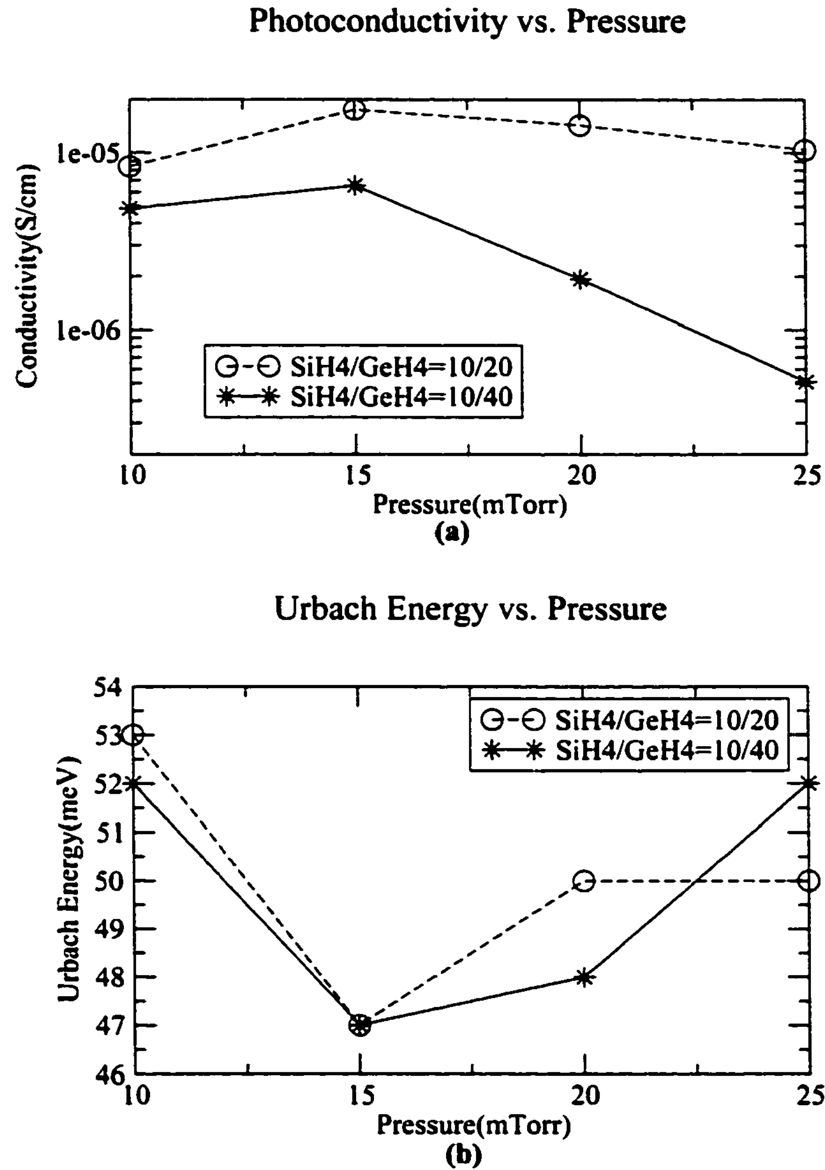

Figure 4.5 (a) The conductivity vs pressure. (b) The Urbach energy vs. pressure. All the parameters were fixed except the pressure.

The regular equation ,

$$\sigma_{ph} = \alpha(1 - R)\phi_{in}q\eta\mu\tau,$$

cannot give a precise value of $\mu\tau$ mainly due to the following reasons: (1) It doesn't take into account the finite thickness limitation, i.e. the thickness interference. (2) It assumes that αd is very small so that $(1 - \exp^{-\alpha d})$ equals αd, which is not true because the incident photon energy is higher than the band gap of the material. In other words, α is above 10^4cm^{-1} while d is around 1-2 μm. Fortunately, the Perkin Elmer Lambda 9 UV/VIS/NIR spectrometer can give precise data on transmission and absorption at a particular wavelength, a simpler equation is then given

$$\sigma_{ph} = \phi_{in}q(1 - R - T)\mu\tau\eta.$$

where R and T are the reflection and transimission coefficient. The thickness interference is already taken into account. Thus, a quite accurate $I_{absorption}$ is obtained. In the above equations, the thickness interference is taken care of by the reflection and transmission coefficient. Any error related to thickness is eliminated. Fig. 4.6 is the $\mu\tau$ product of two series films. This figure further verified that 15 mTorr pressure is better than other pressures. The pressure also affects the growth rate. The growth rate depends on the ionization ratio of reactive gases, the momentum transfer efficiency of the plasma gas, the surface sticking coefficients and the speed of surface hydrogen removal. Higher ion flux due to the low pressure gives rise to higher growth rate (Fig. 4.7). The growth rate keeps increasing with decreasing pressure until the depletion of reactive gases.

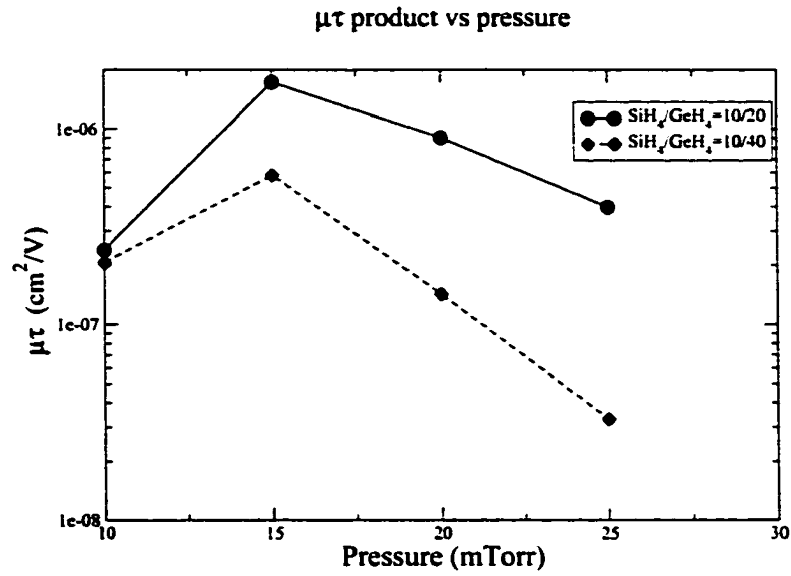

Figure 4.6 $\mu\tau$ product vs pressure

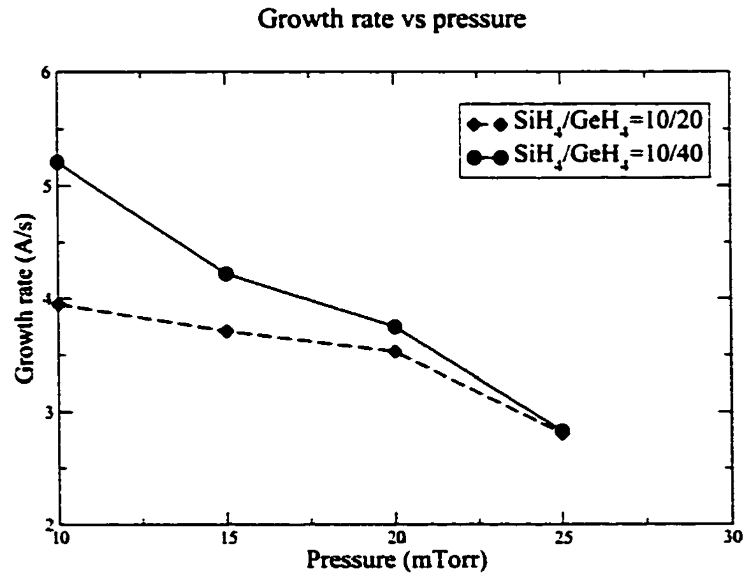

Figure 4.7 Growth rate vs pressure

The Langmuir probe results showed that the ion potential changes with pressure, which will affect the dissociation of reactive gases. The Si-H bond is stronger than the Ge-H and needs more energy to break. With a low-pressure plasma, the preferential dissociation of silane to germane is improved by higher plasma potential and more Si incorporated into the alloy, so the band gap increases. Fig. 4.8 shows that the band gap always increases with decreasing pressure. Another factor that has impact on the band gap is the species of the plasma. The observation of wagging peak shift in the FTIR results, which was mentioned before, tells us that He plasma material has a higher band gap. This is because the helium ions are more energetic than the hydrogen, so that more Si-H breaks up. Another reason, also mentioned before, is that the elimination of clustered Ge could also boost the band gap. The clustered Ge in the bulk could absorb more low energy photons and make the band gap of the films 'look' lower.

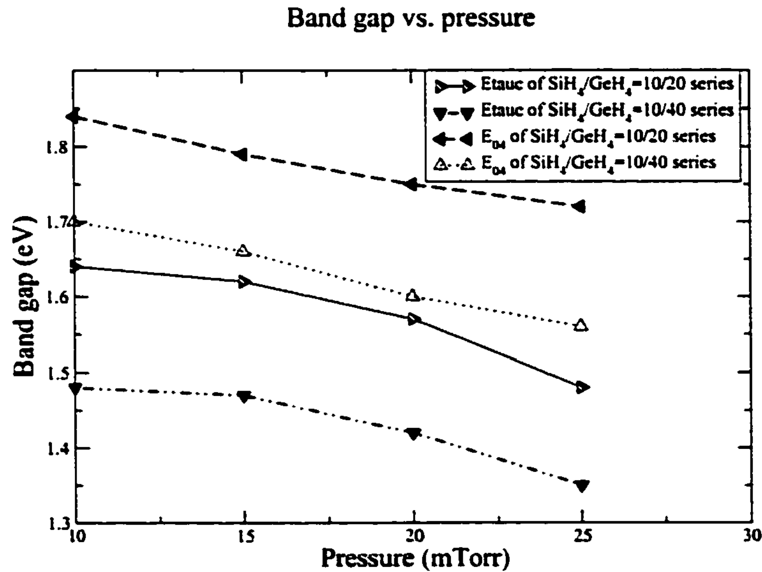

Figure 4.8 Pressure vs band gap. E04 as well as Etauc are given in this graph

4.2.2 The effect of substrate bias

Unlike the conventional CVD system, application of voltage on the substrate would not severely affect the plasma because in an ECR-CVD system the plasma is generated remotely. However, the biased substrate will repel or attract the radicals and ions since they are positively charged. The growth rate, as well as the properties of the materials, is subjected to the changing of substrate bias. Table 4.3 shows several series of samples grown under different bias conditions.

Table 4.3 Deposition parameters for biased substrate investigation

Sample #	Temp ^0C	Pres (mTorr)	Power (W)	H_2 (%)	He (%)	SiH_4 (%)	GeH_4 (%)	Bias (V)
5065	250	10	150	20	50	20	60	-10
5066	250	10	150	20	50	20	60	-20
5067	250	10	150	20	50	20	60	10
5068	250	10	150	20	50	20	60	20
5074	250	10	150	20	50	20	60	40
5076	250	10	150	20	50	20	60	0
5069	250	10	150	20	50	15	60	20
5070	250	10	150	20	50	15	60	-20
5071	250	10	150	20	50	15	60	-10
5072	250	10	150	20	50	15	60	10
5075	250	10	150	20	50	15	60	40
5077	250	10	150	20	50	15	60	0
5184	300	5	150	60	0	15	25	0
5185	300	5	150	60	0	15	25	30
5186	300	5	150	60	0	15	25	20
5187	300	5	150	60	0	15	25	10
5188	300	5	150	60	0	15	25	-10
5189	300	5	150	60	0	15	25	-20
5190	300	5	150	60	0	15	25	30

Fig. 4.9 shows the growth rate change with the bias. As a comparison, the result from pure hydrogen dilution is shown in the same table as well. Theoretically, the growth rate is mainly influenced by two factors: the incident flux of radicals and the incident ion flux. Heavier incident plasma species impinging on the surface could remove the

surface H easily, so the growth rate increases (V. Dalal's model). In Fig. 4.9, the growth rate of the hydrogen dilution plasma has only a small change. It slightly increases with decreasing of bias voltage. Our group's previous research showed that the growth rate changed a lot only under very high voltage. For the helium dilution plasma, however, the growth rate does not change monotonically with bias. Still, we could see that it decreases with high positive bias and increases with high negative bias. The negative bias accelerates plasma species and increases the plasma energy and eventually makes the growth rate shoot up. However, the momentum increase of the incident ions might impinges on the surface heavily and sputter off the radicals at already bonded on the surface, which hinders the further growth rate shooting up. Since the hydrogen ions are very light, this sputtering effect is negligible. What we see is just the monotonic trend.

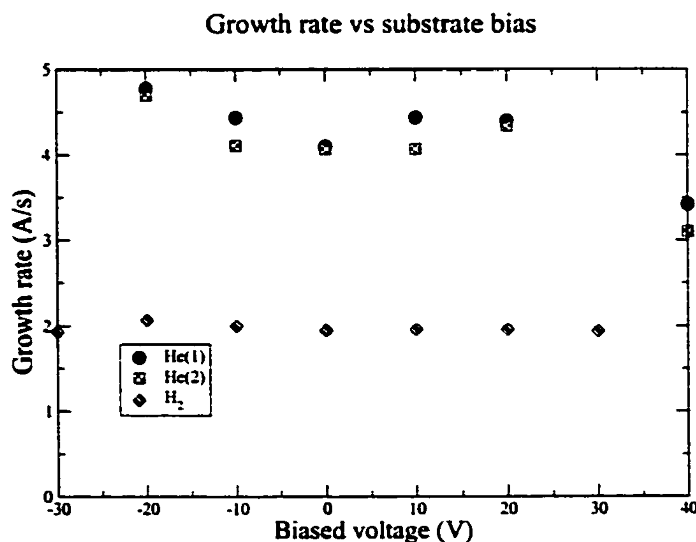

Figure 4.9 The growth rate vs substrate bias

The Space-Charge Limited Current(SCLC) measurement results are depicted in Fig. 4.10. Similarly, the hydrogen dilution results showed a monotonically trend. The

defect density decreases with the addition of ion bombardment. It indicates that in a pure hydrogen plasma, ion bombardment is not enough. More energy is needed to break the hydrogen bonds, clustered Ge, and improve the surface mobility. This is also verified by Zhiyang Zhou's result [26]. The helium dilution result is different. The defect density reaches a minimum with moderate positive bias. This tells us that at 10 mTorr the ion bombardment due to the energetic helium ions is more than enough if the substrate is not biased. 10 mTorr growth condition was not optimal. In previous section, several measurements showed that 15 mTorr is better than 10 mTorr. In terms of ion bombardment, 15mTorr has the proper amount of bombardment.

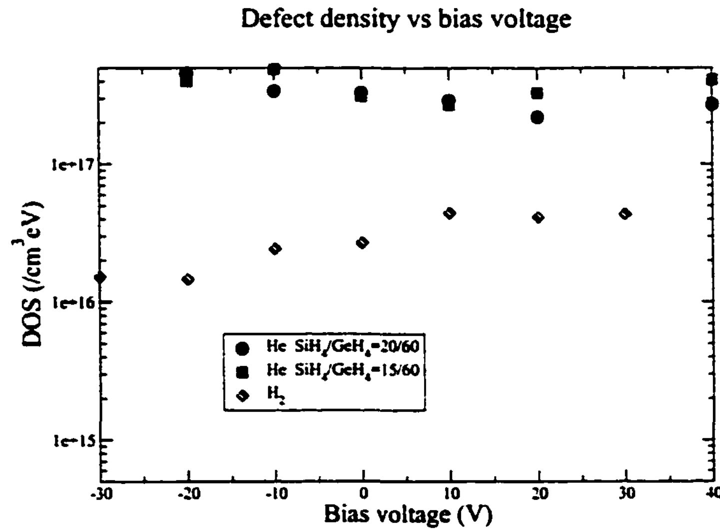

Figure 4.10 The defect density vs substrate bias

4.2.3 The properties of the 15mTorr a-(Si,Ge):H material

Compared to the 10 mTorr results, 15 mTorr still gives us around 5Å/s growth rate. The material grown under this condition has better properties, namely, lower defect density, higher $\mu\tau$ product, lower Urbach energy, high photoconductivity. Most of the comparisons are given in previous sections. The following graphs are the summary of

the properties of 15 mTorr materials. These samples were grown at 15 mTorr, with 50% He and 10% H2 dilution. All the parameters are fixed except the GeH_4 flow ratio in order to vary the band gap. As a comparison, the properties of films without H_2 dilution are also depicted in the graphs(Fig. 4.11, Fig. 4.12, Fig. 4.13, Fig. 4.14).

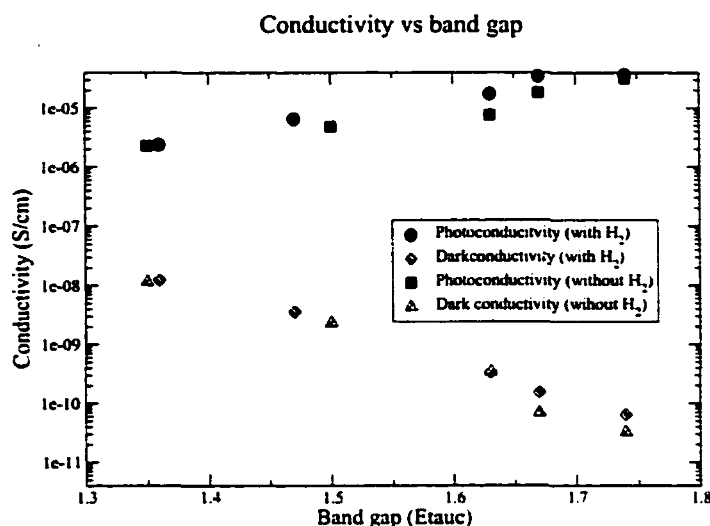

Figure 4.11 Conductivity vs band gap

We could see from the graphs that films deposited without H_2 have degraded properties because they don't have the beneficial effect of the subsurface hydrogen etch. However, too much H_2 could severely decrease the growth rate. We found that 10% H_2 flow rate is enough, since germanium itself can bring in some hydrogen, since it is diluted in H_2 gas. To our surprise, for the band gap (Etauc) from 1.7 to 1.37 eV, the Urbach energy and defect density do not change too much. This indicates that we could get high performance a-(Si,Ge):H solar cells with a germanium content of more than 50%. We have difficulty in making very high Ge-content materials. This is still in process. Researchers in NREL also encountered the same problem when they tried to get low-gap a-(Si,Ge):H films with HWCVD. As has been pointed out in the introduction chapter, it is widely accepted that there are three types of defects: the bond length and bond angle

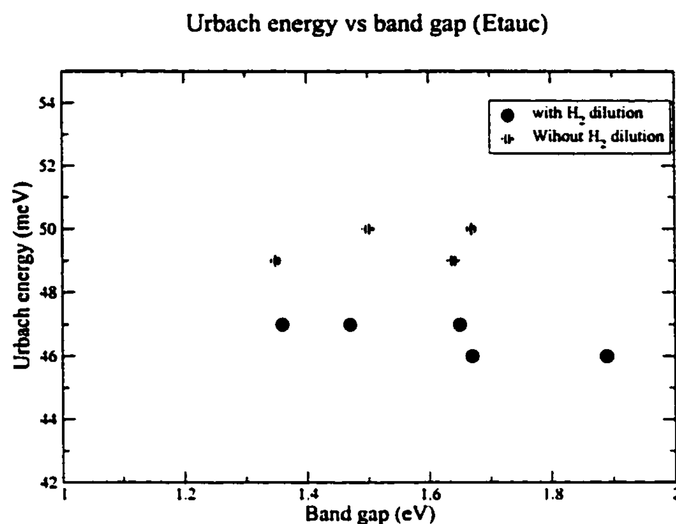

Figure 4.12 Urbach energy vs band gap

distortion, the midgap defect density and the microstructure, although they are strongly correlated. Subgap absorption, SCLC and FTIR measurements are the three methods in our lab to deal with these defect characterizations, respectively. All of these kinds of defects affect the electrical transport properties of the materials. Conductivity measurement as well as the $\mu\tau$ are the tool of gauging the comprehensive effect of the three types of defects. This could explain the fact that the conductivity and $\mu\tau$ product drop more prominently than the Urbach energy and midgap defect density in the Fig. 4.11 4.12 4.13 4.14.

Unlike a-Si:H , high growth rate a-(Si,Ge):H alloying caught researchers' attention only in recent years and only a few data are published. The results of the best films are scattered in the literatures and few people gave a comprehensive list of all the properties obtained which makes it very hard to compare. Generally, the criteria for qualifying a-(Si,Ge):H materials are the properties of films with optical band gap around 1.5 eV where the Ge content is about 40-60%. This is theoretically supposed to be the worst case of alloying. The photo-to-dark conductivity ratio of our films at 1.47 eV band gap

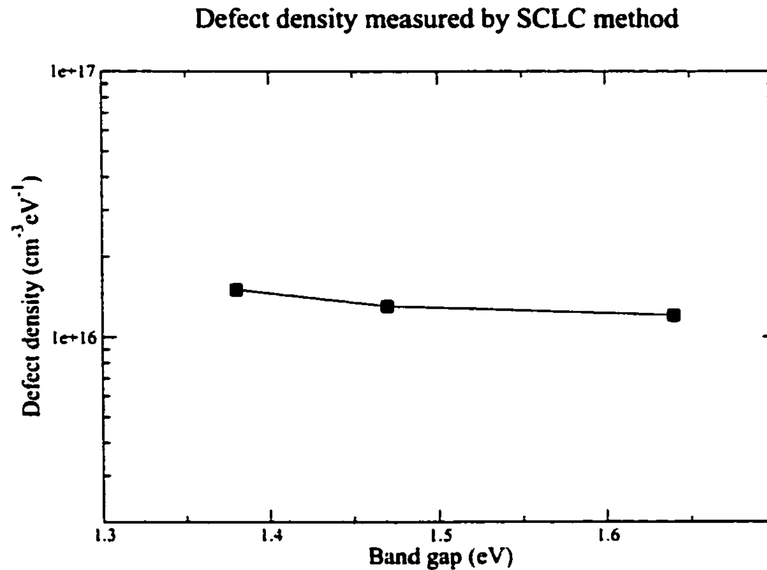

Figure 4.13 Defect density vs band gap

is around 1.83 × 10^3 S/cm. This figure is as good as the best films made by PECVD at regular deposition rate(>1Å/s) [60, 61], but inferior to the very high-hydrogen-dilution films (very low growth rate) [61]. It is better than the high-growth-rate deposition result using HWCVD [62] in NREL. The best result for photoconductivity at Etauc=1.5 eV is around 2.0E-5 S/cm for RFCVD [66], while our result is 1.83E-5 S/cm at a band gap of 1.47eV. The defect density of our films is around 1.1 to 1.5 × 10^{16}cm^{-3}eV^{-1} which is much better than Hegedus' [63] result ($3 \times 10^{16}\ cm^{-3}eV^{-1}$). Our $\mu\tau$ for a band gap of 1.47 eV is 5.8 × 10^{-7}cm^2/V, which is also superior to most of the regular-deposition results [60, 65].

4.3 Results of the a-(Si,Ge):H devices

The devices were made on stainless steel without a back reflector. In order to minimize the cross contamination, a 0.53-0.55 μm n^+ layer was deposited in a RF PECVD

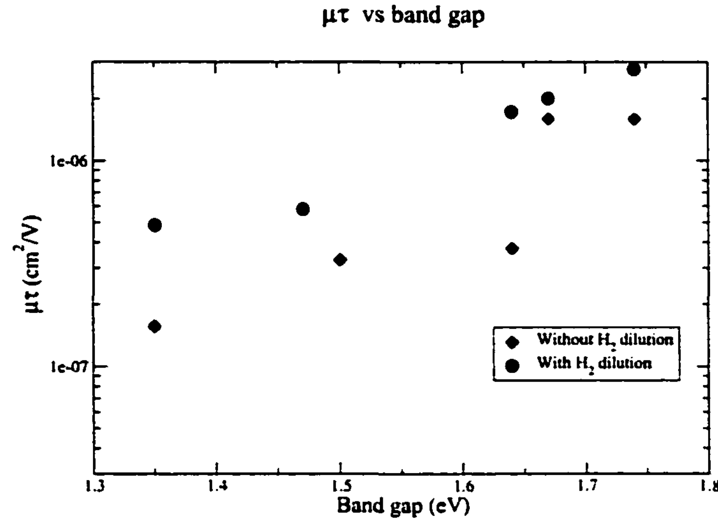

Figure 4.14 Mobility life-time product vs band gap

reactor first and then moved into the ECR-PECVD system for the critical i and p^+ layer deposition. The parameters for the device fabrication were come from the best films we made in the previous stage. i.e. All the devices were grown at 15 mTorr with 10% H_2 and 50% He flow. Graded band gap and graded doping techniques were also used to improve the performance of the a-(Si,Ge):H solar cells. Some of the devices we made in listed in Table 4.4.

Table 4.4 Deposition parameters for high growth rate a-(Si,Ge):H devices

sample	SiH_4 (%)	GeH_4 (%)	TMB (%)	Thickness (μm)	Isc mA	Voc V	FF (%)
2-5582	10	40	10	0.75	.31	.58	64.6
2-5583	10	60	10	0.74	.45	.49	60
2-5584	10	20	10	0.74	.26	.71	71
2-5585	10	0-40	0-40	0.75	.34	.62	71
2-5588	10	80	10	.88	.46	.43	54
2-5593	10	0-60	0-60	.75	.44	.56	68.7
2-5594	10	0-80	0-60	.74	.48	.42	60

The first observation was the open voltage shrinking with the band gap. This is

shown in Fig. 4.15. The open voltage decreases linearly with decreasing band gap. This is because of the smaller band gap drop between the i layer and p^+ layer. For a certain wavelength, when the band gap drops, the absorption increases. Thus more carriers are generated. In Table 4.4, for the same thickness of i layer, the current monotonically increases when more germanium is put into the device. In the previous section, we have said that the properties of a material degrades when more germanium is incorporated into the alloy. As a consequence, the fill factor decreases with shrinking band gap. This is shown in Fig. 4.16.

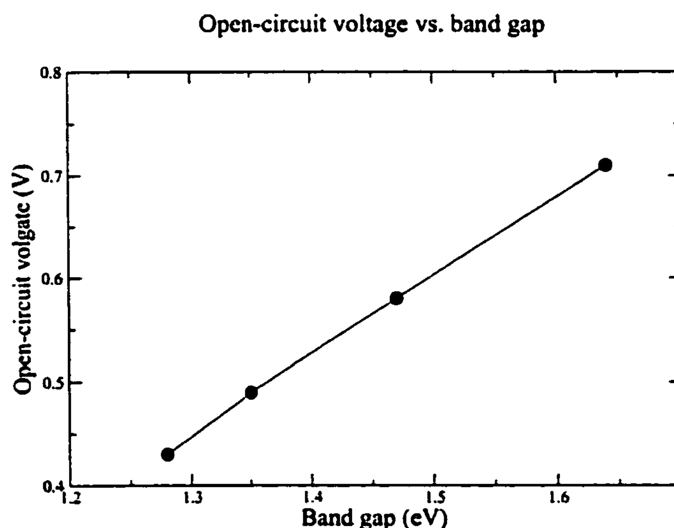

Figure 4.15 The open-circuit voltage changed linearly with band gap. The thickness of the i layer and other deposition conditions except for the germane gas flow were kept as constant as possible to make sure that the open voltage only depends on the band gap.

Quantum efficiency curves of sample 5582 are shown in Fig. 4.17(A). Fig. 4.17(B) is the quantum efficiency at 420 nm and 700 nm. Higher Ge content enhanced the longer wavelength absorption. In summary, with more germanium incorporated into the devices,

1. The open voltage drops due to the band gap shrinking of the i layer when more

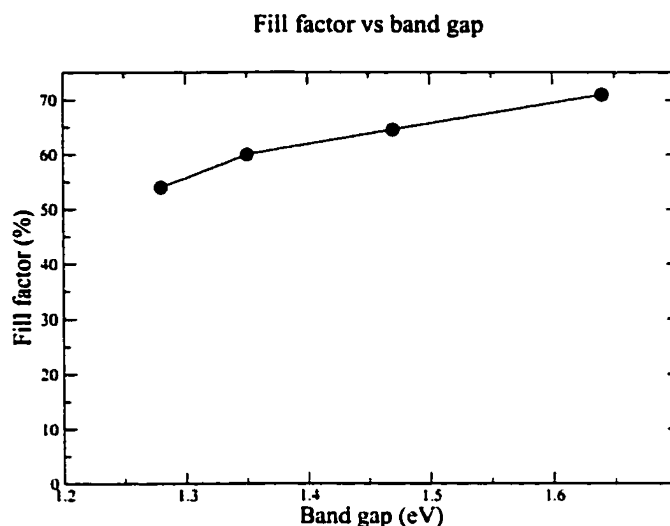

Figure 4.16 The device performance drops due to the degradation of the materials

Ge is put in.

2. The fill factor drops due to the degraded properties of a-(Si,Ge):H .
3. The photo-current increases because of the higher absorption coefficient.
4. The peak value in quantum efficiency shifts to longer wavelength.

In the effort to get high-performance a-(Si,Ge):H solar cells, graded band gap as well as graded doping techniques were used in this work. The band gap diagram was shown in Fig. 4.18. The wide-gap a-Si:H was deposited first on the n-layer and then the decreasing band gap a-(Si,Ge):H . This structure helps hole collection by placing the narrowest band gap near the p-i interface. The holes generated in the worst materials do not need to travel far to the p-layer. Therefore, this design improves the hole collection. Note that the quality of the materials degrades when more Ge is incorporated into the film. To further improve the internal electric field, graded doping was also used. This tilts the band and make it steeper. The dashed line in Fig. 4.18 shows the band diagram for the non-graded-doping profile.

Samples 2-5585 and 2-5593 in Table 4.4 show that graded band gap devices are superior to non-graded band gap devices, especially when the Ge content is very high. For example, 2-5593 has a fill factor of 68.7% while 2-5582 and 2-5583 have less than 65%. The I-V curves and quantum efficiency curves of both 2-5585 and 2-5593 are shown in Fig. 4.19 and Fig. 4.20. The quantum efficiency curves under forward bias are also given. From the graphs we could see that even under forward bias, the quantum efficiency does not decrease too much, which means that the internal electric field is very strong and there is still a big margin for improvement. For example, we could increase the thickness of the i layer to get higher current while maintaining high fill factor. Researchers in NREL and United Solar Corp. [19] had also gotten high-growth-rate graded band gap a-(Si,Ge):H solar cells. Their best device had the band gap graded from 1.75 eV (pure a-Si:H) to 1.55 eV with a fill factor of less than 68%. In this research, the devices we fabricated have graded band gaps to as low as 1.37 eV, while still maintaining a good fill factor of above 68%. This makes more efficient tandem solar cells possible since they could absorb more low energy photons.

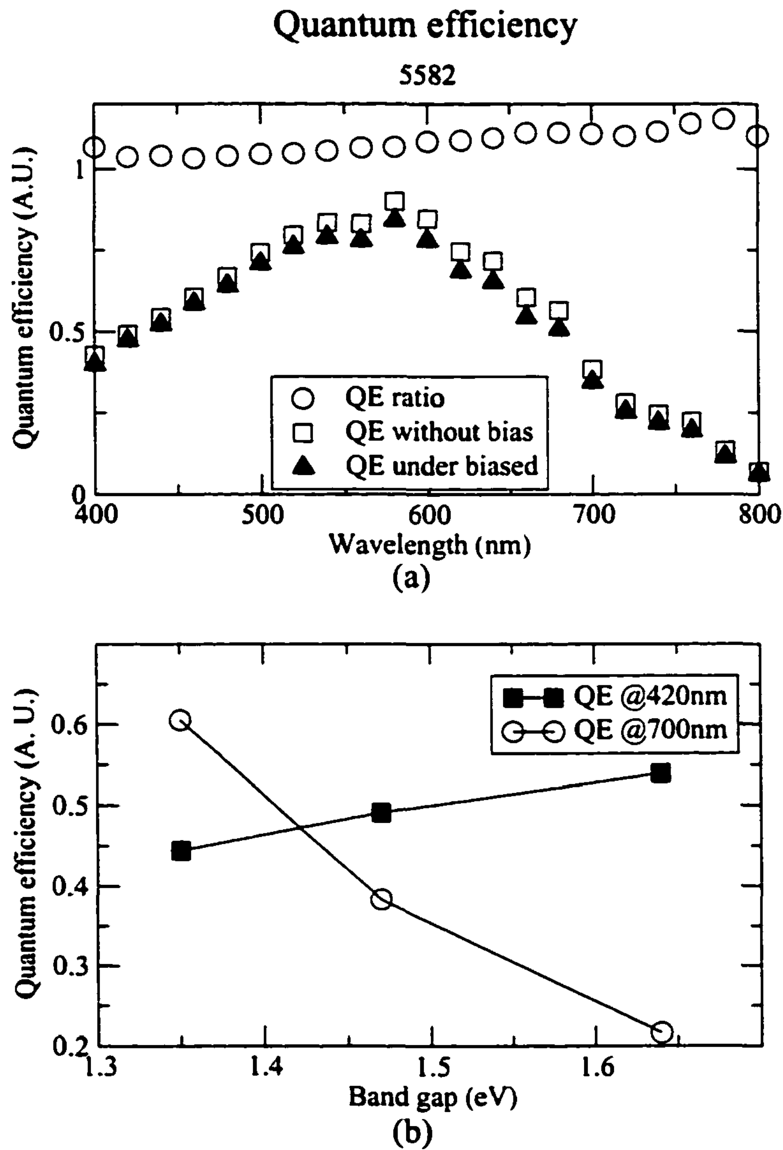

Figure 4.17 (a) Quantum efficiency and quantum efficiency ratio of sample 5582 which has band gap of 1.47 eV. (b) The quantum efficiency of devices at 420 nm and 700 nm. With more Ge incorporated into the devices, the quantum efficiency at longer wavelengths becomes larger.

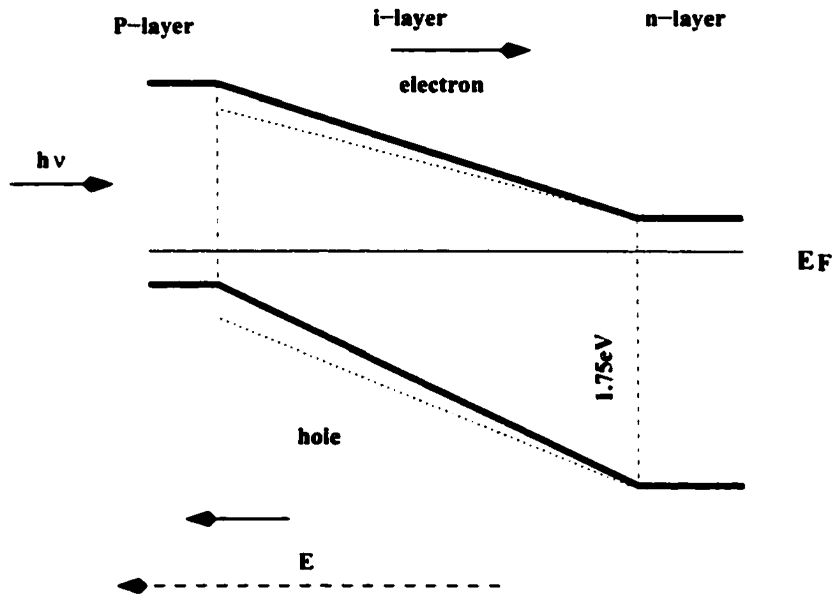

Figure 4.18 Band diagram of graded band gap and graded doping a-(Si,Ge):H p-i-n solar cells. Solid line is with both graded band gap and graded doping, dashed line is only graded band gap.

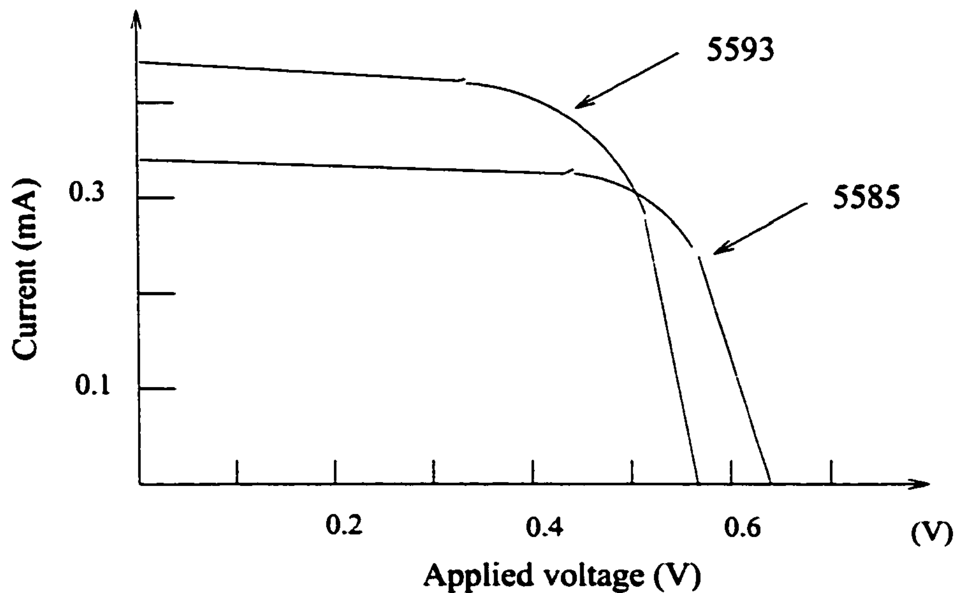

Figure 4.19 I-V curves of samples 5585 and 5593

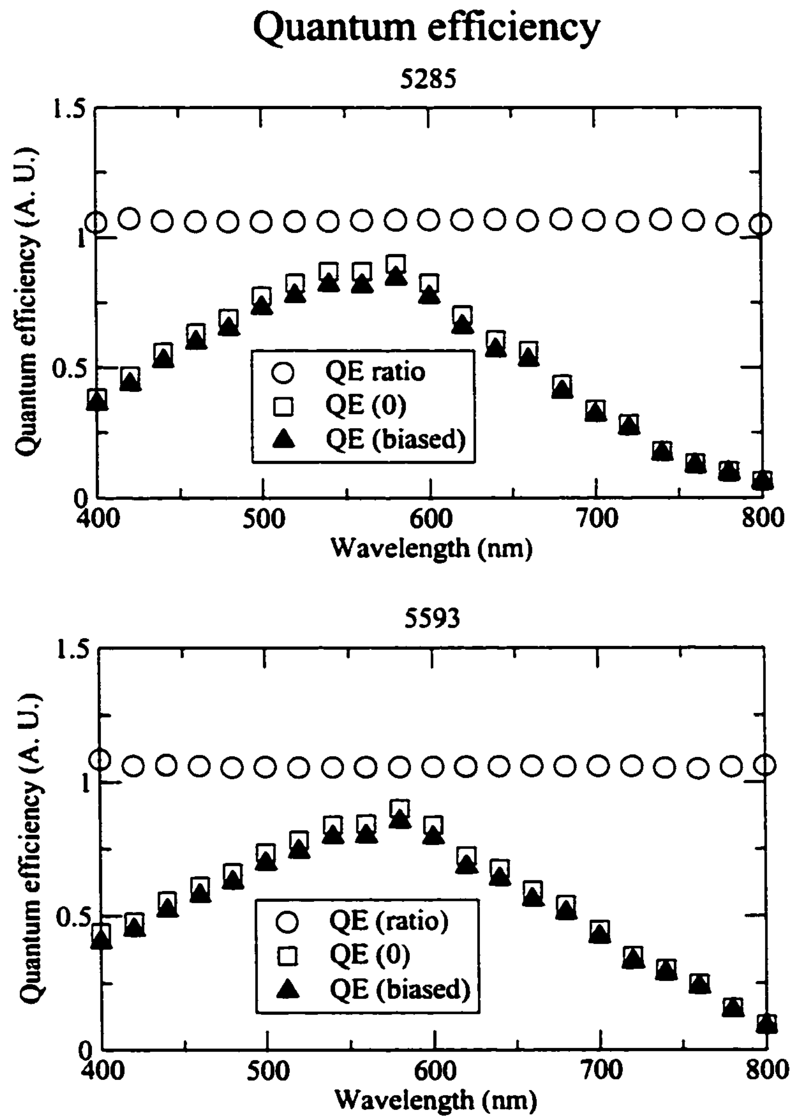

Figure 4.20 The quantum efficiency of samples 5585 and 5593

CHAPTER 5. CONCLUSION

In this work, we have shown how to make high-quality a-(Si,Ge):H films and high-performance a-(Si,Ge):H devices with high growth rate by using the ECR-PECVD deposition technique. Previous work in our group has shown that the ECR technique, using a hydrogen dilution plasma, can be used to deposit good a-(Si,Ge):H films and devices. We have extended this work to the fabrication of high quality a-(Si,Ge):H with high growth rate, and have shown that the devices made from these films are even better than those made by the normal growth rate with hydrogen dilution.

In order to investigate the microstructure and hydrogen content of a-(Si,Ge):H films, FTIR measurements were intensively used during this work. For the first time, we found that the hydrogen content of a-(Si,Ge):H films grown with a high growth rate (helium dilution) is not less than in the normal growth rate material. We also observed the Ge-H stretch mode with high-growth-rate materials. The preferential Si-H attachment to Ge-H is around 2-3, which is less than the figure from the films grown with a normal PECVD system (around 5), and much less the hotwire-CVD films (larger than 10). We also noticed that the dihydride mode (around 2100 cm^{-1}) disappeared with inert gas dilution. All of this observation are cross-verified by themselves and indicates that we have made very good a-(Si,Ge):H materials.

Our group's previous work found that negative bias can provide higher ion bombardment and improve the quality of the films. And the growth rate is also increased because of the higher ion energy. For the helium plasma, we found that sometimes the ion bombardment is more than enough. Positive ion bombardment is not necessary at

10 mTorr. Properly positively biased substrates in 10 mTorr could improve the quality of films. Our films grown at 10 mTorr are inferior to our 15 mTorr films.

We also found that a small amount of H_2 added to the inert gas helium improves the quality of films. This is because H_2 can yield a subsurface etch and reconstruction while pure He cannot. Our conductivity, Urbach energy and $\mu\tau$ measurements all verified that hydrogen-diluted films are better than non-diluted films. For the a-(Si,Ge):H films made at 15 mTorr with 10% H_2 dilution, the defect density from SCLC measurement is below 3×10^{16} $\mathrm{cm}^{-3}\mathrm{eV}^{-1}$, the $\mu\tau$ is above 4×10^{-7} cm^2/V and the Urbach energy is around 47 meV.

Very high performance devices were made in the final stage. The device we made with a 1.47 eV bandgap has a fill factor 64%! With the graded bandgap and graded doping techniques, a 70% fill factor were achieved when the bandgap was graded from 1.75 ev to 1.47 eV. We also got a 68% fill factor with the bandgap graded from 1.75 to 1.38 eV.

In summary, we have succeeded in growing high quality a-(Si,Ge):H material with high growth rate in an ECR system. High performance a-(Si,Ge):H solar cells were also successfully made with these materials.

BIBLIOGRAPHY

[1] Arun Madan, Melvin P. Shaw, "The Physics an Applications of Amorphous Semiconductors", Academic Press, Inc. San Diego, California (1988)

[2] K. D. Mackenzie, J. R. Eggert, et al. "Structural, Electrical and Optical Properties of $\alpha - Si_{1-x}Ge_x : H$ and Inferred Electronic Band Structure", Phys. Rev. B **31**, 2198 (1985)

[3] G. Lucovsky, S. S. Chao., et al., "Chemical Bonding of Hydrogen and Oxygen in Glow-discharge-deposited Thin Films of $\alpha - Ge : H$ and $\alpha - Ge : (H, O)$", Phys. Rev. B, **31**, 2190 (1985)

[4] W. Luft and Y. Tsuo, "Hydrogenated Amorphous Silicon Alloy Deposition Processes", Marcel Dekker, Inc., New York (1993)

[5] M. Stutzmann, R. A. Street, C. C. Tsai, et al. "Structual, Optical and Spin Properties of Hydrogenated Amorphous Silicon Germanium Alloys", J. Appl. Phys. **66**(2), 15 (1989)

[6] D. Adler, "Semiconductors and Semimetals", **21**, Academic Press, New York, 1984

[7] R. W. Collins and J. M. Cavese, "Process Monitoring for a-Si:H Materials and Interfaces", Mat. Res. Soc. Symp. Proc., **118**, 19 (1988)

[8] A. Mahan, P. Raboisson, and R. Tsu, "Influence of Microstructure on the Photoconductivity of Glow Discharge Deposited Amorphous SiC:H and Amorphous SiGe:H Alloys", Appl. Phys. Lett., **50**, 335 (1987)

[9] C.M. Fortmann and J. C. Tu, "Defects in Amorphous Silicon Germanium Alloys", Proc. 20th IEEE PVSC, 139 (1988)

[10] S. Ghua, J. S. Payson, et al., "Fluorinated Amorphous Silicon-Germanium Alloys Deposited from Disilane-Germane Mixture", J. Non-Cryst. Solids, **97&98**, 1455 (1987)

[11] V. L. Dalal, S. Haroon, Z. Zhou, T. Maxson and K. Han, "Influency of Plasma Chemistry on the Properties of a-(Si,Ge):H Alloys", Journal of Non-Crystalline Solids, **266-269**, 675 (2000)

[12] M. Cardona, "Vibrational Spectra of Hydrogen in Silicon and Germanium", Phys. Stat. Sol.(b) **118**, 463 (1983)

[13] J. Yang and S. Guha, "Double-junction Amorphous Silicon-based Solar Cells with 11% Stable Efficiency", Appl. Phys. Lett., **61**, 2917 (1992)

[14] Xixiang Xu, Jeffrey Yang, Subhendu Guha, "Hydrogen Dilution Effects on a-Si:H and a-(Si,Ge):H Material Properties and Solar Cell Performance", Journal of Non-Cryst. Solids, **198-200**, 275 (1996)

[15] A. Matsuda, K. Yagii, M. Koyama, et al., "Preparation of Highly Photosensitive Hydrogenated Amorphous Si-Ge Alloys using a Triode Plasma Reactor", Appl. Phys. Let., **47**(10), 1061 (1985)

[16] V. Dalal, T. Maxson, and S. Haroon, "Influence of Plasma Chemistry on the Properties of Amorphous(Si,Ge) Alloy Devices", Mat. Res. Soc. Symp. Proc., **507**, 441 (1998)

[17] T. Nishimoto, M. Takai, M. Kondo, and Am Matsuda, "High Rate Deposition of Micro and Polycrystalline Silicon", 28th IEEE PVSC at Anchorage Alaska, 876 (2000)

[18] H. Matsumura, "Catalytic Chemical Vapor Deposition (CTL-CVD) Method to Obtain High Quality Amorphous Silicon Alloys", Mat. Res. Soc. Symp. Proc., **118**, 43 (1988)

[19] Q. Wang, Eugene Iwaniczko, et al., "High-Quality 10 Å/s Amorphous Silicon Germanium Alloy Solar Cells by Hot-Wire CVD", Mat. Res. Soc. Symp. Proc., **664**, A7.5 (2001)

[20] V. L. Dalal, T. Maxson, and K. Han, "Properties of a-Si:H and a-(Si,Ge):H Solar Cells Prepared using ECR Deposition Techniques", Conference Record of the IEEE Photovoltaic Specialists Conference Proceedings of the 1997 IEEE 26th Photovoltaic Specialists Conference, Anaheim, CA, 695 (1997)

[21] S. Sugiyama, X. Xu, J. Jiang, and S. Guah, "Light Induced Degration of Amorphous Silicon-Germanium Alloy Solar Cells Deposited at High Rates", Mat. Res. Soc. Symp. Proc, **420**, 197 (1996)

[22] X. Xu, J. Yang, and S. Guha, "Effect of Ion Bombardemnt during Deposition of Amorphous Silicon and Silicon-Germanium Alloy Solar Cells", Journal of Non-crys. Solids, 198 (1996)

[23] A. R. Middya, et al., "Improvement in the Properties of a-(Si,Ge):H Films: Roles of Deposition Rate and Hydrogen Dilution", J. Appl. Phys. **73**, 9 (1993)

[24] A. R. Middya and S. Ray, "Influence of Deposition Rate and Hydrogen/Helium Dilution on the Structural Relaxation of a-(Si,Ge):H Network Prepared at Low Substrate Temperature", J. Appl. Phys., **75**, 11 (1994)

[25] H. Matsumura, "High-quality Amorphous Silicon Germanium Produced by Catalytic Chemical Vapor Deposition", Appl. Phys. Lett., **51**(11), 804 (1987)

[26] Zhiyang Zhou, "The Effect of Ion Bombardment and Low Bandgap a-(Si,Ge):H and a-Ge:H Devices", Ph.D. thesis, Iowa State University, (2000)

[27] S. Matsuo and M. Kiuchi, "Low Temperature Deposition Apparatus Using an Electron Cyclotron Resonance Plasma", Proc. Symp. VLSI Sci. Technol. Electrochemical Soc., Pennington, NJ, 83 (1983)

[28] V. L. Dalal and S. Haroon, "Influence of Plasma Chemistry on the Properties of Amorphous (Si,Ge) Alloy Devices", Mat. Res. Soc. Sym. Proc. Amorphous and Microcrystalline Silicon Technology-1998 Proceedings of the 1998 MRS Spring Meeting. Apr 14-17, San Francisco, CA, 441 (1998)

[29] V. L. Dalal, T. Maxson, and K. Han, "Properties of a-Si:H and a-(Si,Ge):H Solar Cells Prepared using ECR Deposition Techniques", Conference Record of the IEEE Proceedings of 1997 IEEE 26th PVSC, Anaheim, CA, 695 (1997)

[30] G. Baldwin, V. Dalal, and K. Han, "Deposition of High Quality a-(Si,Ge):H Films and Novel Graded Gap Devices Using RF Triode Glow Discharge Deposition", Conference Record of the IEEE proceedings of the 23rd IEEE PVSC, Louisville, KY, 1037 (1993)

[31] V. L. Dalal, "Some Considerations Relating to Growth Chemistry of Amorphous Si and (Si,Ge) Films and Devices", Mat. Res. Soc. Sym. Proc. **664**, A5.2 (2001)

[32] V. L. Dalal, "Fundamental Considerations Regarding the Growth of Amorphous and Microcrystalline Silicon and Alloy Films", J. Non-Cryst. Solids, **395**, 173 (2000)

[33] V. L. Dalal, S. Kaushal and K. Han, "A Critical Review of the Growth and Properties of a-(Si,Ge):H ", Photovoltaic Energy Conversion, Conference Record of the 24th IEEE PVSC, (1994)

[34] A. Mahan, Y. Xu, B.P. Nelson, et al., "Saturated Defect Densities of Hydrogenated Amorphous Silicon Grown by Hot-Wire Chemical Vapor Deposition at Rates up to 150 Å/s", App. Phys. Lett., **78**(24), 3788 (2001)

[35] S. Guha, J. Yang, Scott J. Jones, Yan Chen, and D. Williamson, "Effect of Microvoids on Initial and Light-Degraded Efficiencies of Hydrogenated Amorphous Silicon Alloy Solar Cells", App. Phys. Lett., **61**, 1444 (1992)

[36] Y. S. Tsuo, Y. Xu, I. Balberg, and Richard S. Crandall, "Effects of Helium Dilution on Glow Discharge Depositions of a-(Si,Ge):H alloys", Proc. 22nd IEEE Photovolt. Spec. Conf. 1334 (1991)

[37] A. Matsuda, M. Koyama, N. Ikushi, et al., "Guiding Principle in the Preparation of High-photosensitive Hydrogenated Amorphous SiGe Alloys from Glow-Discharge Plasma", Japn. J. Appl. Phys. **25**, 54 (1986)

[38] J. Perrin, M. Shiratani, K. Patrick, et al., "Surface Reaction Probabilities and Kinetics of H, SiH_3 , Si_2H_5, CH_3 and C_2H_5 during Deposition of a-Si:H and a-C:H from H_2, SiH_4, and CH_4 Discharges", J. Vac. Sci. Technol. A, **16**(1), 278 (1998)

[39] A. Gallagher, "Neutral Radical Deposition from Silane Discharges", J. Appl. Phys., **63**(7), 2406 (1988)

[40] S. Perkowitz, "Optical Characterization of Semiconductors", Academic Press, New York, (1993)

[41] J. Tauc, "Optical Properties of Solids", North-Holland, Amsterdam, (1970)

[42] K. Seeger, "Semiconductor Physics, an Introduction", Springer-Verlag, New York, (1991)

[43] F. Urbach, "The Long-wavelength Edge of Photographic Sensitivity and the Electronic Absorption of Solids", Phys. Rev. 92 (1953)

[44] H.P. D. Lanyon, "Electrical and Optical Properties of Vitreous Selenium", Phys. Rev. **130**, 134 (1963)

[45] S. Al. Jalali, G. Weiser, "Electroabsorption studies on amorphous silicon", J. Non Cryst. Solids, **41**, 1 (1980)

[46] S. Lee, S. Kumar, and C. Wronski, "A Critical Investigation of a-Si:H Photo Conductivity Generated by Sub-gap Absorption of Light", J. Non-Cryst. Solids, **114**, 316 (1989)

[47] M. H. Brodsky, M. Cardona, and J. J. Cuomo, "Infrared and Raman Spectra of the Silicon-Hydrogen Bonds in Amorphous Silicon Prepared by Glow Discharge and Sputtering", Phys. Rev. B, **16**, 3556 (1977)

[48] H. Shanks, C.J. Fang, L. Ley, M. Cardona, et al., "Infrared Spectrum and Struture of Hydrogenated Amorphous Silicon", Phys. Stat. Sol. (b), **100**, 43 (1980)

[49] A. A. Langford, M. L. Fleet, and B. P. Nelson, et al. " Infrared Absorption Strength and Hydrogen Content of Hydrogenated Amorphous Silicon", Phys. Rev. B. **45**, 13367 (1992)

[50] N. Maley and I. Szafranek, "Amorphous Silicon Technology", Mat. Res. Soc. Sym. Proc., **192**, 663 (1990)

[51] S. M. Sze, "Physics of Semiconductor Devices", 2nd Edition, John Wiley & Sons, Inc. New York, (1981)

[52] R. S Crandall, "Modeling of Thin Film Solar Cells: Uniform Field Approximation", J. Appl. Phys. **54**(12), 7176 (1983)

[53] S. Haroon, "Effect of Deposition Condition on Properties of a-(Si,Ge):H Films and Devices Using ECR-Plasma Deposition", ISU thesis, (1998)

[54] K. D. Mackenzie, P. G. Le Comber, and W. E. Spear, "The Density of States in Amorphous Silicon Determined by Space-Charge-Limited Current Measurements", Philosophical Magazine B, **46**(4), 377 (1982)

[55] W. Den Boer, "Determination of Midgap Density of States in a-Si:H Using Space-Charge-Limited Current Measurements", Journal De Physique, **42**, C4, 451 (1981)

[56] R. L. Weisfield, "Space-Charge-Limited Currents: Refinements in Analysis and Applications to $a - Si_{1-x}Ge_x : H$ Alloys", J. Appl. Phys., **54**(11), 6401 (1983)

[57] N. Maley and I. Szafranek, "Amorphous Silicon Technology", MRS Symp. Proc. **192**, 663 (1990).

[58] W. Paul, D. K. Paul, et al., "Preferential Attachment of H in Amorphous Hydrogenated Binary Semiconductors and Consequent Inferior Reduction of Pseudogap State Density", Phys. Rev. Lett., **46**, 1016 (1981)

[59] Brent P. Nelson, et al., "Techniques for Measuring the Composition of Hydrogenated Amorphous Silicon-Germanium Alloys", J. Non-Cryst. Solids. ICAMS 18, (2000)

[60] W. Paul and K. Mackenzie, "Amorphous Hydrogenated Silicon Germainum Alloys Suitable for Photoelectronic Applications", Annual Subcontract Report, 1 July 1985-30 June 1986, SERI/STR-211-3107, Golden, CO: Solar Energy Research Inst, (1987)

[61] S. Wagner, et al., "The Optoelectronic Properties of a-(Si,Ge):H (F) Alloys", Mat. Res. Soc. Symp. Proc. Pittsburgh, PA, **118**, 623 (1988)

[62] P. B. Nelson, Y. Xu, et al., "Hydrogenated Amorphous Silicon Germanium Alloys Grown by the Hot-Wire Chemical Vapor Deposition Technique", Mat. Res. Soc. Symp. Proc. MRS., San Francisco, **507**, 447 (1998)

[63] S. Hegedus, et al. "Low Bandgap Amorphous Silicon-germanium Alloys for Thin Film Solar Cells Using a Novel Photo-CVD Reactor", Proc. 19th IEEE PVSC, 867 (1987)

[64] S. Hegedus, R. Rocheleau, et al., "Photo-Assisted CVD of a-(Si,Ge):H Solar Cells and a-(Si,Ge):H Films", Proc. 20th IEEE PVSC, 129 (1988)

[65] K. Mackenzie, et al., "Comparison of the Structural, Electrical and Optical Properties of Amorphous Silicon-Germanium Alloys Produced from Hydrides and Fluorides", Phys. Rev. B, **38**, 6120 (1988)

[66] W. Luft, "Characteristics of Hydrogenated Amorphous Silicon-Germanium Alloys", Appl. Phys. Comm., **9**, 43 (1989)

ACKNOWLEDGEMENTS

First and foremost, my sincere gratitude goes out to my major professor Dr. Vikram Dalal for his invaluable guidance and support throughout this research project. I would also like to thank Dr. David Lynch, Dr. Gary Tuttle, Dr. Joseph Shinar and Dr. Rebert Weber for serving on my committee. Thanks also go out to Kay Han and Max Noack for assistance in the laboratory and for sharing their expertise with experimental work.

I would like to thank Xi Huang and Zhiyang Zhou for getting me oriented in MRC. Jason Zhu, Andy Liu, Young Huh for their help with film and device characterization, Roger Keen and Paul Seebeger for cleaning substrates, Curtis Sell for instrument trouble shooting. I would also like to thank Jane Woillne, Masela Pontoh, Qi Chen, Tris Tanadi, Adam Sanford, Jason Herold, Tim Maxson for their assistance, advice and friendship.

Finally, I would like to thank my wife, Irene and my families for their patience, support and love during this educational and time consuming experience.